UNIVERSITY OF LATVIA

FACULTY OF PHYSICS, MATHEMATICS AND OPTOMETRY

Edgars Butanovs

SYNTHESIS AND PROPERTIES OF TRANSITION METAL DICHALCOGENIDE BASED CORE-SHELL NANOWIRES

SUMMARY OF DOCTORAL THESIS

Submitted for the Doctoral degree in Physics
Subfield of Materials Physics

Riga, 2020

The doctoral thesis work was carried out in Institute of Solid State Physics, University of Latvia from 2016 to 2020.

The thesis contains an introduction, 5 chapters and a reference list.

Form of the thesis: dissertation in materials physics

Supervisor: *Dr.phys.* **Boris Polyakov**, senior researcher

Reviewers:

1. *Dr.habil.phys.* **Linards Skuja**, senior researcher, Institute of Solid State Physics, University of Latvia

2. *Dr.sc.ing.* **Andris Šutka**, senior researcher, Riga Technical University

3. *Dr.sci.* **Alexey Romanov**, professor, ITMO *University* (Saint Petersburg, Russia)

The thesis will be defended at the public session of the Doctoral Committee of Physics, Astronomy and Mechanics of University of Latvia on September 11, 2020 in the conference hall of Institute of Solid State Physics, 8 Kengaraga street.

The thesis is available at the Library of the University of Latvia, Raiņa blvd. 19.

Chairman of the Doctoral Committee *Dr.habil.phys.* **Uldis Rogulis**

Secretary of the Doctoral Committee **Karlīna Engere**

ISBN 978-9934-18-548-9

ABSTRACT

This Dissertation is dedicated to the development and characterization of various material nanowire (NW) and transition metal dichalcogenide *core-shell* heterostructures.

Novel synthesis methods of highly-crystalline *core-shell* NWs have been demonstrated, the nanomaterials structure, composition, morphology and photoelectrical properties have been characterized. The following results can be highlighted:

- Synthesis of novel ZnO-WS_2 *core-shell* NW heterostructures. Fabrication of as-grown nanostructure single-nanowire photodetector and demonstration of enhanced photoelectric properties in comparison to pure ZnO NWs.
- Synthesis of novel GaN-ReS_2, ZnS-ReS_2 and ZnO-ReS_2 *core-shell* NW heterostructures. Development of new few-layer ReS_2 synthesis method – sulfurization of a pre-deposited ReO_x coating.
- Synthesis of novel ZnO-MoS_2 *core-shell* NW heterostructures by decomposition and sulfurization of a pre-deposited $(NH_4)_6Mo_7O_{24}\cdot 4H_2O$ coating, and comparison with sputter-deposited MoO_3 coating conversion.
- Synthesis of novel PbI_2-decorated ZnO NW heterostructures. Development of new few-layer PbI_2 synthesis method – iodination of a pre-deposited PbO_x coating. Fabrication of as-grown nanostructure single-nanowire photodetectors and demonstration of their photoelectric properties.

The synthesis methods developed in this work are not limited to the demonstrated heterostructures and can be applied for other materials. Furthermore, this work provides an insight into how a few-atomic-layer thin coating can change the photoelectric properties of a ZnO nanowire.

Keywords: nanowire, transition metal dichalcogenide, 2D materials, zinc oxide, photodetector, nanofabrication

CONTENTS

1. INTRODUCTION

1.1 Problems and motivation

Nanowires (NWs) – 1D nanostructures – are being explored as promising materials for applications in electronics, optoelectronics, photonics and microelectromechanical systems (MEMS), and their potential has been demonstrated in many proof-of-concept devices [1]. Depending on the application, two different approaches of NW integration in devices can be distinguished – single-NW devices consist of individual separate NWs as the active components, whereas "bulk" devices contain periodic NW arrays or randomly dispersed NWs. Some NW applications, mainly the single-NW devices, struggle in assembly and scalability of the device fabrication to create a cost-effective production process that could compete with current technologies, such as silicon microfabrication. Several concepts have been proposed, for instance, controlled printing of NWs with roll-to-roll technology that uses microfluidics to align the NWs [2]. However, many other NW applications are entirely novel or complementary to current technologies and might be implemented in a much more scalable fashion, which is presently an active research field. Otherwise, entirely new applications or device concepts need to be proposed and developed. The necessary scientific research is not only related to developing competitive upscaling methods but also to producing new NW-based materials and studying their fundamental properties for novel applications [3]. One way to enhance and engineer NW characteristics, such as spectral absorption range and electrical properties, is to create *core-shell* heterostructures – to modify the surface of a NW by a relatively thin coating (compared to the diameter of the NW) of a different material [4]. Surface of NWs has a significantly reduced lattice mismatch restriction compared to conventional semiconductor thin film growth thus enabling greater flexibility in choosing the materials to produce heterostructures and in engineering their properties [5,6].

Layered 2D van der Waals (vdW) materials have attracted great interest since the isolation of monolayer graphene in 2004 due to their unique structure and the promising physical properties that appear when the thickness of the material is reduced to one atomic layer [7]. Transition metal dichalcogenides (TMDs) are layered materials with a general chemical formula MX_2, where M is a periodic table Group 4 – 7 transition metal and X is a chalcogen, and are being actively researched for applications in electronics and optoelectronics due to their thickness-dependent bandgap [8]. TMDs layers have terminated surfaces without dangling bonds and are bound together by weak vdW forces, therefore, can be sequentially stacked unstrained without any covalent interlayer bonding even if materials are slightly lattice-mismatched [9]. There is an on-going search for large-scale synthesis methods of TMDs on different substrates before any practical applications could be realized [10].

Combining NWs and TMDs in *core-shell* heterostructures could lead to new knowledge about the interface formation between different materials and solid-state reactions in such systems, to novel nanostructures with enhanced properties, and development of new TMDs synthesis methods as NWs are a convenient template to study materials growth.

1.2 Objective and tasks

The main objective of this work is to synthesise novel *core-shell* nanowire heterostructures based on semiconductor nanowires and transition metal dichalcogenides, and to characterize the synthesised materials.

The following tasks have been defined:

1. To synthesise different material semiconductor NWs by *vapour-liquid-solid* (VLS) method and explore the potential of using such together with different TMDs in *core-shell* heterostructures.

2. To develop or adapt different methods of growing highly crystalline few-layer TMDs around NWs by chemical conversion of a pre-deposited coating.

3. To characterize as-grown nanostructures to obtain information about their structure, composition, morphology and optical properties, and use it to tune the growth process.

4. To test some selected synthesized materials for fabrication of single-nanowire photodetector devices, and to determine their photoelectric properties.

5. To assess the role of the shell on the NW photoelectric properties, and evaluate the potential of using such heterostructures in different practical applications.

1.3 Scientific novelty

The work summarized in this Dissertation encompasses new knowledge on synthesis of several different few-layer TMDs and on preparation of novel *core-shell* NW heterostructures, and includes elaboration on their physical properties. The following results can be highlighted:

1. Development of a versatile two-step method for growth of various layered vdW materials on semiconductor NWs. The procedure consists of deposition of a sacrificial coating on NWs via sputtering or immersion which is afterwards chemically converted in a reactive vapour at elevated temperature. In this work, highly-crystalline WS_2, ReS_2, MoS_2 and PbI_2 shells were successfully grown on monocrystalline NWs. The synthesis method is not limited to the demonstrated *core-shell* heterostructures but can also be applied for other materials.

2. Investigation of photoelectric properties of the selected novel as-grown heterostructures. ZnO-WS_2 *core-shell* NW two-terminal devices exhibit enhanced spectral responsivity up to 7 A/W at 405 nm illumination in comparison to pure ZnO NWs, and light absorption in the WS_2 shell extends the active spectral range to the red part of the spectrum. Up to 0.6 A/W high spectral responsivity was measured for the PbI_2-decorated ZnO NW photodetector devices at 405 nm illumination, and significantly decreased dark current was observed in comparison to pure ZnO NWs. Notably, ZnO NW surface passivation with layered vdW materials shell also improves their photoresponse time for almost two orders of magnitude due to thus limited photo-induced processes related to adsorption/desorption of atmospheric oxygen species which typically slows down photoresponse in ZnO NWs.

1.4 Contribution of the Author

The direct contribution of the Author is as follows: growth of NWs via VLS method; development of the sulfurization/iodination processes and tuning of the process parameters for *core-shell* heterostructure synthesis; characterization with scanning electron microscope and X-ray diffraction; single-nanowire photodetector device fabrication including optical lithography, *lift-off* and *in situ* NW manipulations inside SEM-FIB; photoelectric measurements of the as-fabricated devices; analysis and interpretation of the obtained data.

Body of the article was written by the Author for Publications I, III and VI, parts of the article were written by the Author for Publications II and IV.

2. LAYERED 2D TRANSITION METAL DICHALCOGENIDES

Layered 2D van der Waals (vdW) materials have attracted great interest since the isolation of monolayer graphene in 2004 and the Nobel Prize in Physics in 2010, due to their unique structure (strong in-plane bonds and weak interlayer bonding) and the promising physical properties that appear when the thickness of the material is reduced to one atomic layer. Nowadays it is an ongoing wide research field that focuses on many different materials, specific synthesis and characterization approaches, device fabrication and applications [10].

2.1 Properties of transition metal dichalcogenides

Transition metal dichalcogenides (TMDs) can be described by a general chemical formula MX_2, where M is a periodic table Group 4 – 7 transition metal and X is a chalcogen (Group 16 elements S, Se and Te) [7]. The focus of the dissertation is on TMDs, however, lead iodide PbI_2 is also investigated, thus, despite PbI_2 being a metal halide, all of the investigated layered materials henceforth are called TMDs due to their structural similarity and for the sake of convenience. Depending on the group the transition metal belongs to, the TMDs properties can vary significantly. Typically, a TMD monolayer is made of hexagonally-positioned metal atom layer, "sandwiched" between two layers of chalcogen atoms (see *Fig. 2.1*). In the layer metal and chalcogen atoms are connected by strong covalent bonds, while the layers are bound together by weak van der Waals forces. TMDs are chemically quite inert as they have no dangling bonds on the surface due to the fact, that all the electrons in the compound atoms are paired.

The electronic structure of TMDs is dependent on the metal atom coordination and the number of its d-electrons, therefore, they have a broad spectrum of electrical properties [11]. Due to the progressive filling of d bands from Group 4 to Group 7, compounds can exhibit metallic conductivity (orbitals partially filled) or can be semiconductors (orbitals fully occupied). The chalcogen atom affects the electronic structure much less than the metal atom, however a trend can still be observed due to the broadening of the d bands – with an increasing atomic number of the chalcogen the bandgap decreases. Interesting differences in the electronic structure of semiconducting TMDs is observed between bulk and monolayer material due to the

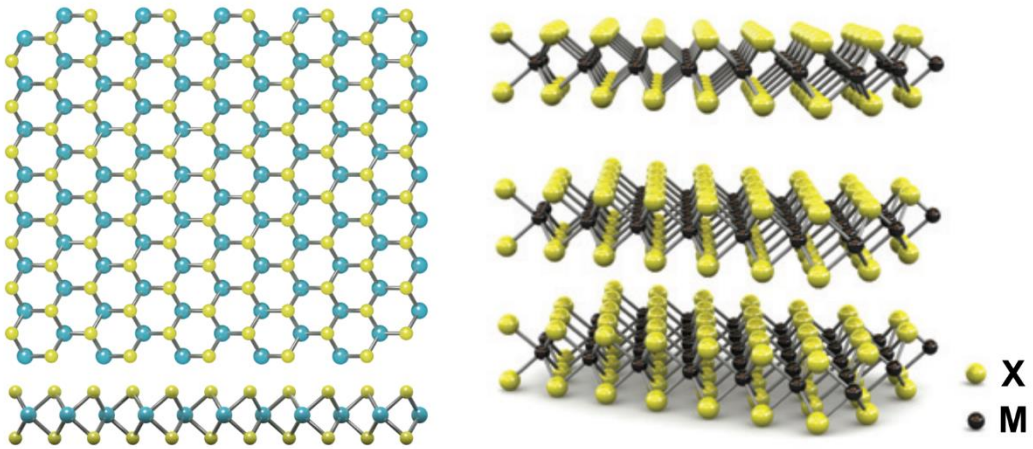

Figure 2.1. A schematic representation of transition metal dichalcogenides atomic

changes in interlayer coupling, symmetry elements and degree of quantum confinement. For instance, bulk MoS_2 is an indirect-bandgap semiconductor with a bandgap around 1 eV with the valence band maximum at Γ point and the conduction band minimum between Γ-K symmetry lines of the Brillouin zone, however a MoS_2 monolayer has a 1.8 eV wide direct bandgap at the K point [12,13]. The direct bandgap of many monolayer TMDs is one of the main reasons for the intensive research done on these materials, because the use of direct bandgap semiconductors is a necessity for an effective operation of optoelectronic devices. On the other hand, there are theoretical and experimental studies that shows band structure shift from direct bandgap to indirect bandgap when the PbI_2 thickness is reduced from bulk to monolayer, therefore monolayer PbI_2 is not expected to be an efficient material for optoelectronics applications [14,15]. Another exception – ReS_2 exhibits much weaker interlayer coupling, therefore it remains a direct bandgap semiconductor in both bulk, few-layer and monolayer forms [16].

For electronic and optoelectronic applications, good electrical and optical properties of the used materials are needed. The variety of available 2D vdW materials allows to fabricate all-2D-material devices, where usually *h*-BN is used as an insulator, graphene as a metal, and TMDs as semiconductors [10]. Most 2D materials have good mechanical properties – their electrical and optical characteristics deteriorate only slightly when bending or applying tensile stress [17]. That allows them to be incorporated in devices on flexible substrates, such as polymers, thus enabling development of wearable, transparent flexible and stretchable electronics in future [18,19]. TMDs are being widely researched for potential applications in electronic and optoelectronic devices as a large portion of the materials are semiconductors with a wide range of bandgaps, starting from visible to infrared. Current limitations of their use in high-performance switching devices is their relatively low carrier mobility. TMDs monolayer strong photoluminescence and large optical absorption makes them promising candidates for different optoelectronics applications, like light-emitting diodes, phototransistors etc. on transparent flexible substrates [8].

2.2 Synthesis methods

It is intuitive, that an isolated TMD monolayer cannot be stable in air just by itself – since a single layer is less than 1 nm thick, vdW forces make it bend, roll and wrinkle, making other types of nanostructures [20]. Therefore, TMDs are either synthesised on top of a supporting substrate or dispersed in a stabilizing liquid.

Top-down methods usually involve bulk material crystal that is being reduced in size, for example cleaved, micropatterned, etched etc., to lower its dimension to 2D. Either mechanical or liquid exfoliation is usually performed. Mechanical exfoliation involves three steps: an adhesive tape is applied on the surface of the available bulk crystal; the tape is peeled of the crystal to obtain thin layers of the material attached to the glue of the tape due to the weak vdW forces between the layers; the tape with the 2D crystals is pressed against the substrate and removed. This cleavage method is relatively simple, fast and cost-effective; however, the monolayer yield of this process is very low, therefore can only be utilized for laboratory scale studies and not for large-scale production [11]. As the process does

not use any chemicals and is only based on the shear force applied on the crystal during the peeling process, high crystallinity is maintained, hence, it is suitable for fundamental studies of the material properties. On the other hand, for low-cost mass production of 2D atomic crystals, solution processing can be utilized [21–23]. Liquid-phase exfoliation involves dispersion of the bulk material in a suitable solvent and a use of ultrasound or ion intercalation to separate individual layers. After the exfoliation process, the resultant suspension can be centrifuged to select crystals of desired thickness and lateral size [24]. A range of printing techniques, inkjet or flexographic for instance, are available to be used in high-volume low-cost production to fabricate devices on either rigid or flexible substrates [25].

Alternatively, bottom-up methods involve combining and stacking material atoms together, and usually these include thermodynamically or kinetically driven processes, such as condensation of vapour. One can use pulsed laser deposition, molecular beam epitaxy or chemical synthesis, however these methods are usually either slow, costly, non-scalable or creates low quality material. The most common bottom-up approach for growing TMDs is chemical vapour deposition (CVD), as it can potentially be scaled up for mass production [26,27]. Several different CVD approaches for growth of TMDs mono- and few-layer 2D crystals can be distinguished. Most commonly used method is a vapour phase reaction between transition metal oxide and chalcogen precursors. Typically, the corresponding metal oxide powder is being evaporated simultaneously with a chalcogen powder in a high-temperature reactor, followed by a vapour-phase reaction to form the corresponding TMDs, which diffuse to the substrate to produce layered 2D crystals [28,29]. However, some transition metal oxides have high melting points (titanium and niobium oxides, for instance), therefore it is difficult to effectively evaporate them. For such materials, transition metal chlorides or oxychlorides can be used instead, as they usually have much lower melting temperatures. Another approach is to directly evaporate TMD powder in a hot zone of the furnace, transport the vapour with a carrier gas to the substrate in the cold zone, where nucleation and crystal growth takes place. The thickness and grain size of the 2D crystals can be controlled by adjusting the growth temperature and time. With the mentioned approaches it is possible to grow single-crystalline domains of various TMD materials, however, the use of solid precursors makes it difficult to precisely adjust the vapour pressure and supersaturation, thus limiting uniform growth over a large area [26,27]. Growth of 2D TMDs over the entire wafer area with a good spatial homogeneity has been demonstrated using metal-organic precursors via the MOCVD technique [30], therefore making it a prospective method for future large-scale production.

Another methodology how to obtain 2D TMD crystals is to convert previously deposited precursor thin films. One commonly used approach involves transformation of a transition metal or transition metal oxide film in chalcogenide vapour at elevated temperatures, where the starting material film has been deposited on the substrate by physical vapour deposition (magnetron sputtering etc.) [31–34]. The benefit of this method is that the wafer-scale TMD thin films can be readily obtained, however, it usually produces polycrystalline films with small grain size due to the amorphous nature of the precursor films. Moreover, thermal decomposition of thiosalts can be used to obtain 2D crystals. For example, to obtain 2D MoS_2 on a

substrate, the substrate is first dip-coated in a $(NH_4)_2MoS_4$ solution, followed by a decomposition at a high temperature, which involves N and H atom disassociation from the substrate and MoS_2 layer growth [35]. There is still an ongoing research on growing a high-quality wafer-scale 2D TMDs with CVD technique as the process is complicated and involves many parameters.

Fabrication of scalable high quality 2D material heterostructures is required for most potential future applications. Direct bottom-up sequential growth of 2D materials on top of each other is currently being investigated as the main heterostructure fabrication method in future due to its scalability [27]. VdW materials, which have terminated surfaces without dangling bonds, therefore, grow without covalent interlayer bonding, may be sequentially grown on top of each other unstrained by "van der Waals epitaxy" due to this weak interlayer vdW interaction, even if materials are lattice-mismatched [9,36,37]. The field of vdW epitaxial growth is still fresh, and a lot of research must be performed to overcome difficulties related to the small lateral size of heterostructure grains, reproducibility, limited yield, as well as more combinations of materials must be studied.

2.3 Perspective applications

2D TMDs are regarded as very attractive for wide range of applications including electronics, optoelectronics and photonics, energy, sensing and piezoelectric devices [8]. The mentioned applications are motivated by the unique properties of 2D TMDs, such as tunable electronic structure, optical transparency, mechanical strength, and sensor sensitivity, some of which mainly arise due to the high surface contribution in monolayer. A particularly interesting and promising application is the use of 2D materials in flexible electronics, which is considered as potentially ubiquitous in future devices in every-day life. Flexible technology merges a variety of scalable devices, such as transistors, displays, solar cells, chemical and mechanical sensors and energy storage on flexible substrates for either large-area applications or compact wearable electronics [18,25].

Regarding this work, 2D TMDs have been demonstrated as good photodetectors, which can be used in imaging, communications, positioning and guidance. Good photodetector characteristics are a small device size, fast response time and high sensitivity over a wide wavelength range [38,39]. Photoresistors and phototransistors (based on photoconductivity, when photo-excited carriers contribute to the current) made from monolayer TMDs, including MoS_2 and WSe_2, exhibit excellent properties such as high responsivity and high quantum efficiency [38,39]. Furthermore, the size-dependent bandgap and the large variety of different TMD materials allows one to control the response spectrum. Photodetection properties of the most common TMDs materials have been studied quite extensively, however, the applications require further in-depth research, and investigation of other less-known compounds.

Currently there still are numerous challenges and issues to be overcome before 2D materials can be used in any practical application, as 2D materials have only been studied for a decade or so. Firstly, it is controlled large-scale growth of 2D heterostructures. Large-scale growth of monolayer TMDs and graphene with satisfactory properties has been demonstrated [26,27], however, direct growth of

heterostructures (several layers of different 2D materials on top of each other) has not, mainly due to the initial choice of the substrate, materials relative thermal stability and complexity of precise control of temperature and gas partial pressures [10]. Currently, either very small scale heterostructures have been grown via CVD or made by dry-transfer technique [40,41]. Secondly, the control of the carrier type and concentration in 2D TMDs which is crucial for industrial semiconductor applications have not yet been fully studied [42]. Material doping or alloying have been investigated as potential methods of modifying electronic properties of the materials [43,44]. Thirdly, ensuring ohmic contacts in semiconductor devices is required for any real application [45,46]. In conventional semiconductors, ion implantation at the metal contact area allows to generate a gradual ion density distribution to reduce the contact resistance, however, the concept is ambiguous and not applicable in 2D materials, therefore, several other methods are being investigated, such as layer phase engineering and use of graphene as an electrode material. The challenges mentioned above are only the few main ones, as many other more specific ones exist in more specialized application fields.

There are some more exotic phenomena observed in 2D materials worth noting, that might be of practical use in future. Spintronics, in contrast to electronics where the signal is transported by a carrier charge, uses the carrier spin information to transport the signal. Materials which have a strong spin-splitting due to some kind of symmetry breaking or non-equilibrium state allow spin-polarized carrier population. Effective spin injection from TMDs to graphene has been demonstrated, therefore such graphene/TMD heterostructures could be used in future spintronics devices. On the other hand, TMDs exhibit different spin characteristics at K and K` points in the electronic band structure due to strong spin-orbit coupling which leads to a possibility to control electrons and their spins at different positions in momentum space [47]. The carriers in these valleys can be spin-selectively controlled by circularly polarized light. Use of these phenomena for a potential information storage and manipulation in future devices has been termed as “valleytronics”, and use of 2D materials in both of these new fields are currently being extensively investigated.

3. NANOWIRES

One-dimensional (1D) nanostructures, such as nanowires (NWs), nanorods, nanobelts and nanotubes, have been extensively studied for more than two decades due to their unique physical properties. Some of the main research directions nowadays are investigations of hybrid NWs and heterostructures [4], development and study of complex photonic and/or plasmonic NW-based integrated circuits [48], metallic NW-based flexible and transparent electrode fabrication [49], and, of course, large-scale assembly of NW devices that could enable mass production [50]. An important emerging phenomenon in NWs research is the need for full understanding not only of the behaviour of each individual component in hybrid materials systems but also the interfaces and interaction between them which determines the performance and properties of the device [1].

3.1 Materials, properties and applications

Generally, functional NWs can be classified into two large groups – metallic and semiconducting, and that determines the perspective applications where such NWs can be applied. Many classes of semiconductor NWs exist: the most well studied elemental semiconductors Si and Ge, III-V compounds (GaN, GaAs, InP etc.), II-VI compounds (CdS, In_2S_3, ZnSe etc.), oxides (ZnO, MgO, SnO_2, ITO etc.) and carbides (SiC) [51]. In this work, different compound semiconductor NWs were studied.

It is important to discuss the unique properties of NWs besides the possible miniaturization, that make them so attractive to study and to compete with the well-developed silicon and thin film technologies. Firstly, their one-dimensionality allows to overcome some technical problems that optically active thin films face in regard to integration with silicon. To merge photonics and electronics on one platform, one must eliminate interfacial lattice mismatch that leads to defective and inefficient optical materials. Secondly, size reduction of well-known materials to nanoscale can alter and improve their physical characteristics and device performance, as well as introduce completely novel properties. Some of the size-dependent properties are photon absorption and emission, charge carrier transport and elastic modulus. Regarding the electronic transport in NWs, single-crystalline structure can be obtained over a length of several micrometres thus eliminating charge carrier scattering on grain boundaries and that promotes good electrical properties, however, if the diameter of a NW is reduced to a value close to electron mean free path, scattering on the surface can become significant. Furthermore, as NWs have large surface-to-volume ratio, both surface and bulk lattice may contribute to the macroscopic properties of a NW. Therefore, NWs might replace bulk materials in an application where surface-dominated property, for instance, surface charge carrier processes in chemical or biological sensing, determines the efficiency or sensitivity of the device. It has been reported in literature that physical characteristics and device performance are particularly sensitive to surface properties in ZnO NWs, as the surface states in ZnO NWs may be affected by atoms and ions from the surrounding atmosphere [52,53].

NWs have been extensively explored as potential building blocks for many different applications as their superior performance in devices has been demonstrated

in comparison to conventional materials. Application fields include field-effect transistors, optoelectronic devices, photonic circuits, chemical sensors, energy storage and conversion. Optoelectronics is one of the most promising areas where semiconductor NWs might be potentially applied. In the context of this work, it has been widely reported that NWs photodetectors exhibit high photosensitivity and photoconductive gain [52,54,55]. Due to the large surface-to-volume ratio of NWs, they contain very high density of surface states that leads to Fermi pinning near the surface, thus forming a depletion space charge layer that separates electrons and holes and, consequently, enhances photocarrier lifetime. As high mobility can be easily achieved in single-crystalline defect-free NWs grown by VLS, that, in combination with long carrier lifetimes, leads to large photoconductive gain, therefore, making NW photodetectors very promising in different optical applications [56].

3.2 Nanowire synthesis via *vapour-liquid-solid* mechanism

Generally, all NW synthesis methods are grouped in "top-down" and "bottom-up" approaches. Top-down methods typically involve chemical or ion beam etching of a bulk material which has been patterned lithographically. Such process involves several complicated steps including material growth, photoresist deposition/removal, etching, and it becomes gradually more complex for high density NW arrays with small feature sizes, however, the method benefits from precise control over the placement of NWs on a substrate which is necessary for device fabrication at large scale. While bottom-up methods usually lack such control over NW position on a substrate, the approach is much more widely used because it is more versatile, facile and potentially cheaper with great control over NW properties, even if *in-situ* or post-growth alignment methods need to be implemented. Bottom-up approach can be divided in solution-phase and gas-phase methods. Chemical solution-phase methods have been widely applied to grow colloidal NWs, and benefit from large-scale production, control of NW geometry and surface passivation. Gas-phase methods, such as vapour-liquid-solid (VLS), are the most adopted methods for growing semiconductor NWs due to their flexibility and high-quality of the as-grown NWs. In this work, VLS method with a metal nanoparticle (NP) catalyst was used to grow NWs.

The simplified general principle of the VLS method is schematically depicted in *Fig. 3.1*, however, usually the growth involves more steps when several other complex processes may occur which usually depends on the materials used. Generally, the VLS growth of NWs typically consists of three steps: alloying, nucleation and growth. Firstly, the vapour-phase precursors are adsorbed and incorporated into the metal catalyst nanodroplet at elevated temperatures, and an alloy is formed. Depending on the materials used, the chemical reactions between the precursors to obtain NW material may occur either in gas-phase or on the surface of the metal droplet. Secondly, if the alloying process is complete and the precursor supply is maintained, nucleation takes places due to supersaturation, which leads to precipitation of the NW material seed at the liquid-solid interface. Finally, if continuous and uniform vapour flow is supplied, the NW grows in an atomic layer-by-layer fashion in one axial direction, limited by the droplet size, and the growth

front is at the liquid-solid interface. Time and precursor vapour flow (partial pressure) typically determines the growth rate of the NWs, while temperature is set to be above eutectic temperature of the corresponding alloy. The growth temperature may determine the crystal phase of the material, and the phase of the NW can also be imposed by the substrate material if an epitaxial relationship exists.

3.3 *Core-shell* heterostructures

To date, many fundamental properties of pure NWs are well understood. On the other hand, the combination of different materials in more complex hybrid NWs gives extra freedom to flexibly design their properties and add custom-made functionality [4]. Radial or coaxial (commonly called *core-shell*) NWs are heterostructures where the core NW is coated by another material to enhance its characteristics. As the surface of a NW can greatly influence its properties, even a very thin coating might drastically change the performance of the NWs in different device applications.

Core-shell NWs might be categorized in two groups, depending on the function of the *shell* material. The shell can be called active, if it is necessary for the operation of a device, for instance, if a p-n junction is formed between the core and the shell, and there are quite a few reports in literature on semiconductor *core-shell* NW heterostructure electronic and optoelectronic devices [5,57,58]. Otherwise, the shell can be called passive, if it only improves some property of the core NW and it does not directly participate in the operation of the device. There are many reports on modification of NWs mechanical properties [4,59,60] and use of the shell to passivate the surface states of a NW [61], to realize high electrical conductivity NW channels or to protect the NW from atmospheric conditions [4].

Core-shell NW fabrication methods mainly vary depending on the desired functionalities needed. Typically, the shell is formed in two step or multistep processes when either growth parameters or the synthesis method is changed. During CVD process, it is possible to switch from axial VLS growth mode to radial mode by changing the temperature and/or precursors, thus obtaining either a differently doped or a different material shell [62,63]. Otherwise, after the VLS growth of NWs, deposition method should be changed. Atomic layer deposition is an excellent method for precisely controllable deposition of amorphous oxides, such as SiO_2 and Al_2O_3, that are used for surface passivation, enhancement of mechanical properties and wrap-around gate dielectrics. Other thin film deposition methods, such as pulsed laser deposition and molecular beam epitaxy, have been used to deposit semiconductor materials directly on the NWs [64,65]. To grow uniform and highly

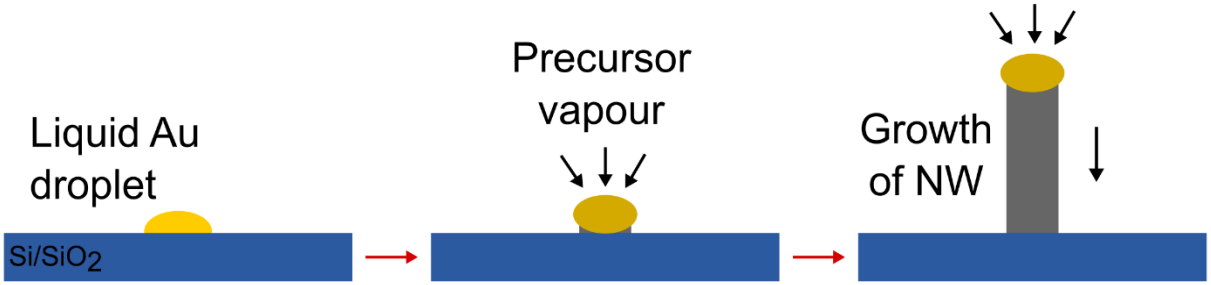

Figure 3.1. A schematic representation of *vapour-liquid-solid* growth mechanism.

crystalline shell with thin film deposition methods for semiconductor heterostructure applications, lattice parameters of both core and shell materials should be considered.

In this work, semiconductor materials *core-shell* NWs with layered TMDs shell were synthesised. Such novel heterostructures could be used for applications in optoelectronics and photo- or electrocatalytic hydrogen evolution reactions. There have been very few articles in literature on fabrication of similar *core-shell* nanostructures [66–70] and promising properties have been demonstrated, therefore, the scope of the Thesis is to extend this field by exploring new materials combinations and complementary synthesis methods, and investigating the heterostructure applicability in optoelectronics and catalysis.

4. EXPERIMENTAL METHODS

4.1 Physical vapour deposition

In physical vapour deposition (PVD), by physically ejecting atoms or molecules from a target material, thin film grows when they condense and nucleate on the surface of the substrate. *Sidrabe SAF25/50* multifunctional cluster tool was utilized in this work. Thermal evaporation has been used in this work for depositing thin 5 nm/45 nm Cr/Au electrodes on the SiO_2/Si substrate, where Cr layer is used to enhance Au adhesion to the surface. Different transition metal oxide coatings, such as WO_3, MoO_3, ReO_x, PbO_x, were obtained by reactive DC magnetron sputtering. Typically, 100 W DC power was used with different Ar/O_2 partial pressures and sputtering times, depending on the material.

4.2 Chemical vapour deposition

Chemical vapour deposition (CVD) is defined as a method of growing thin films or coatings by a dissociation and/or chemical reactions of vapour-phase precursors in an activated environment. Here, CVD was mainly used in two cases: NW growth via VLS mechanism, and sulfurization/iodination of transition metal oxide coatings; thermally activated atmospheric pressure CVD system with a horizontal quartz tube reactor was utilized.

All of the NWs mentioned in this work were synthesised via VLS method (see *Chapter 3.2*). To synthesise a layered material shell around a NW, typically a pre-deposited metal oxide coating was converted by a sulfurization/iodination reaction. Sulfur/iodine vapour was obtained by evaporating the corresponding powder in the necessary temperature and delivered to the sample by the carrier gas. By placing the sample in the required temperature, solid-state reaction occurs when the vapour diffuses into the oxide shell and reacts with it. By adjusting the temperature, one controls the diffusion rate, thus the degree of the crystallinity of the shell.

4.3 Electron microscopy

Scanning electron microscopes (SEM) uses relatively lower energy electrons to obtain information about the surface morphology from secondary and/or backscattered electrons. One of the greatest benefits of SEM is a wide depth of field at large range of magnifications in combination with high resolution. SEM is an essential tool in this work for imaging synthesised NWs and nanostructures (*Lyra, Tescan* SEM was used). Furthermore, built-in focused ion beam (FIB) with a gas injection system (GIS) was used for *in-situ* single-NW device fabrication.

In contrast to SEM, transmission electron microscopes (TEM) reveals the inner atomic structure of the studied material. Atomic resolution is often obtained, thus giving some information about the crystal structure - phase, lattice constant and plane orientation. In this work, TEM (*Tecnai GF20, FEI)* was used to visualize synthesised NW *core-shell* heterostructures and to determine the thickness of the shell layer, as the difference between core and shell can be clearly distinguishable.

In a TEM, high-energy electrons due to their short wavelength can be used to study crystallographic properties of a material as its atoms may diffract them. The resulting image on the TEM screen is a pattern of bright spots – selected area

diffraction (SAED) pattern, where each spot corresponds to a certain diffraction condition of the crystal structure. Here, diffraction patterns were analysed using CrysTBox software [71], which allows automatic spot identification, reciprocal lattice construction and crystal phase matching.

4.4 X-ray diffraction and spectroscopy methods

X-ray diffraction (XRD) is a powerful method of analysing materials structure. In this work, XRD was utilized to determine the phase composition of the synthesised samples using *Rigaku MiniFlex 600* X-ray powder diffractometer with Bragg-Brentano θ-2θ geometry and Cu anode X-ray tube (Cu $K\alpha$ radiation, λ = 1.5406 Å).

Raman spectroscopy – inelastic scattering of monochromatic light – can be used to determine the chemical structure of a material. In this work, micro-Raman measurements were performed using a confocal microscope with spectrometer *Nanofinder-S (SOLAR TII)*. Confocal microscopy allows to locate nanostructures on a substrate and focus the laser beam to around 1 μm diameter, thus it is possible to measure Raman spectra of single NWs and NW heterostructures. Many TMDs exhibit relatively strong Raman scattering, therefore, micro-Raman spectroscopy is a powerful technique to identify thin layers of TMDs on nanostructures, as have been demonstrated in this work.

Optical luminescence spectroscopy is used to investigate the optical properties of the material of interest. In this work, mostly semiconductor materials with a bandgap width in the visible spectrum are studied, therefore photoluminescence measurements give information about the width of the optical bandgap and defect bands.

4.5 Optical lithography

Here, a direct-write laser photolithography (*μPG101, Heidelberg Instruments*), followed by metallization and *lift-off*, was used to obtain gold microelectrode pattern on oxidized silicon wafers. Firstly, a positive photoresist layer is coated on a SiO_2/Si substrate by *spin-coating* technique. Secondly, the resist is exposed to light which follows a pattern design, and a chemical developer is applied to remove the exposed resist. Thirdly, 5 nm/45 nm Cr/Au film is deposited on top of the patterned substrate by a thermal evaporation. Finally, to remove the unwanted metal film, *lift-off* is performed by immersing the substrate in a specific organic solvent, that dissolves the underlying resist and thus the unnecessary metal film detaches from the substrate. As-prepared metal electrodes are large square electrodes that are needed to attach macroscopic contacts with two long “arms” with a gap width of 2 μm where a NW is subsequently placed on top.

4.6 Single-nanowire device fabrication and photoelectric measurements

In this work, NWs were *in-situ* mechanically placed on top of the pre-defined electrodes with a nanomanipulator inside a SEM-FIB. Firstly, a single NW from the substrate is welded to the tungsten nanomanipulator probe using electron-beam-assisted platinum (Pt) deposition, where Pt metalorganic is delivered by GIS. Afterwards, the NW is aligned and placed on top of the electrodes, welded with Pt

deposition to ensure an electric contact and fixed position, and cut off from the nanomanipulator probe with gallium ion beam.

As-prepared single-NW devices were characterized as two-terminal photodetectors. Current−voltage ($I-V$) characteristics and photoresponses to light of different wavelengths were measured with two-contact microprobe station connected to a low-noise current preamplifier (*SR570, Stanford Research Systems*) and oscilloscope (*TDS2004B, Tektronix*). 405 nm, 532 nm and 660 nm wavelength semiconductor diode lasers with the power of 0.5 W/cm^2 were the illumination sources. Optical beam shutter (*Thorlabs SH05*) was used for time-resolved measurements; all the measurements were performed at room temperature and in air. *LabView*-based software was developed to control the experimental setup.

5. RESULTS AND DISCUSSION

5.1 ZnO-WS_2 *core-shell* nanowires

Tungsten disulfide WS_2 is an indirect bandgap semiconductor material with a 1.3 eV gap, however, when reduced to monolayer, the gap becomes direct and shifts to around 1.9 eV [31]. 2D monolayer WS_2 crystals have been previously grown via several methods, such as CVD [28,72] and pre-deposited WO_3 film sulfurization [31,73]. WS_2 monolayers exhibit high PL quantum yield and decent carrier mobility (up to 200 $cm^2V^{-1}s^{-1}$), therefore have potential applications in future optoelectronics [28,31,74]. In this work, few-layer WS_2 was grown around ZnO and GaN NWs by a simple three-step route: as-grown ZnO and GaN NWs were coated with amorphous WO_3 layer using reactive DC magnetron sputtering, then ZnO- and GaN-WO_3 NWs were annealed in a quartz tube reactor in a sulfur atmosphere at 800°C to convert the oxide coating to WS_2, followed by annealing in N_2 atmosphere to sublimate the remaining WO_3 [75].

As-grown ZnO-WS_2 NWs were first imaged and studied with SEM (see *Fig. 5.1*). The length and diameter of the pure and *core-shell* NWs is in the same range, thus the morphology of NWs is maintained after the heat treatment during the heterostructure preparation. The length of the NWs varies from 10 to 50 μm, the diameter is around 100 nm.

To reveal the NW inner structure, TEM was used (see *Fig. 5.2*). Firstly, Au NPs were located at the end of NWs, which were used as catalysts for VLS growth. Secondly, few-layer WS_2 shell was observed on the ZnO NW surface, and is clearly visible as parallel black lines. The thickness of the shell was 1-5 monolayers (each consisting of S-W-S atomic planes), and the measured interlayer distance was around 6.3 Å, which corresponds to previously reported distance 6.2-6.4 Å in WS_2 nanostructures [76]. Furthermore, the single-crystalline structure of ZnO NW core can be well seen.

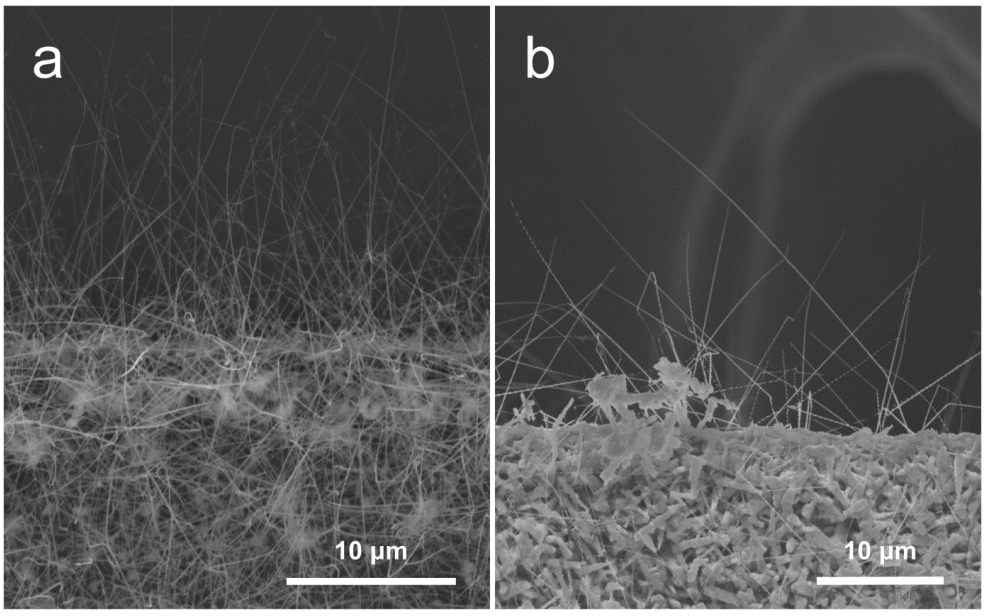

Figure 5.1. SEM images of (a) pure ZnO NWs, and (b) ZnO-WS_2 *core-shell* NWs.

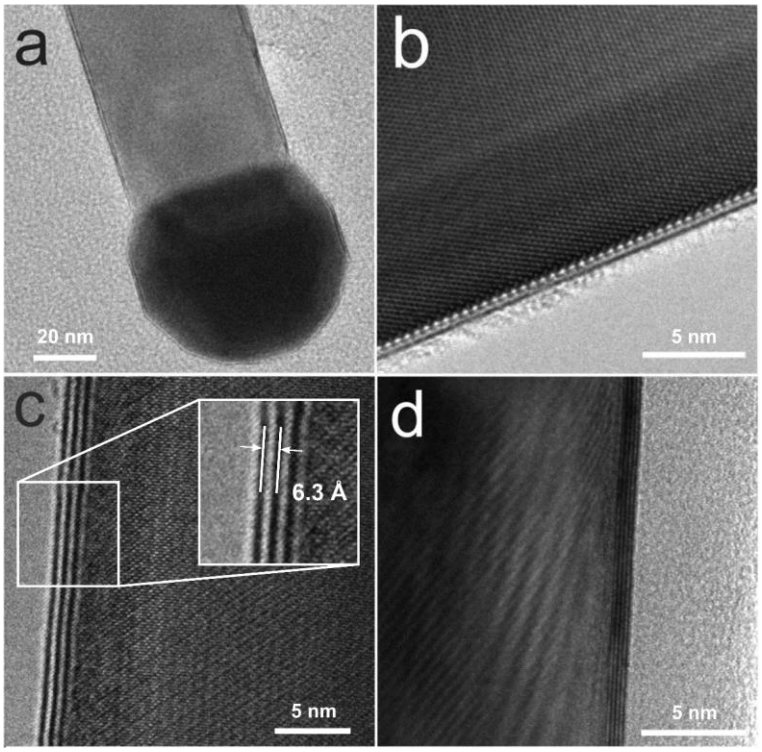

Figure 5.2. TEM images of ZnO-WS_2 *core-shell* NWs. WS_2 can be distinguished as parallel black lines on the NW surface. The inset shows the measured atomic interlayer distance in the WS_2 shell.

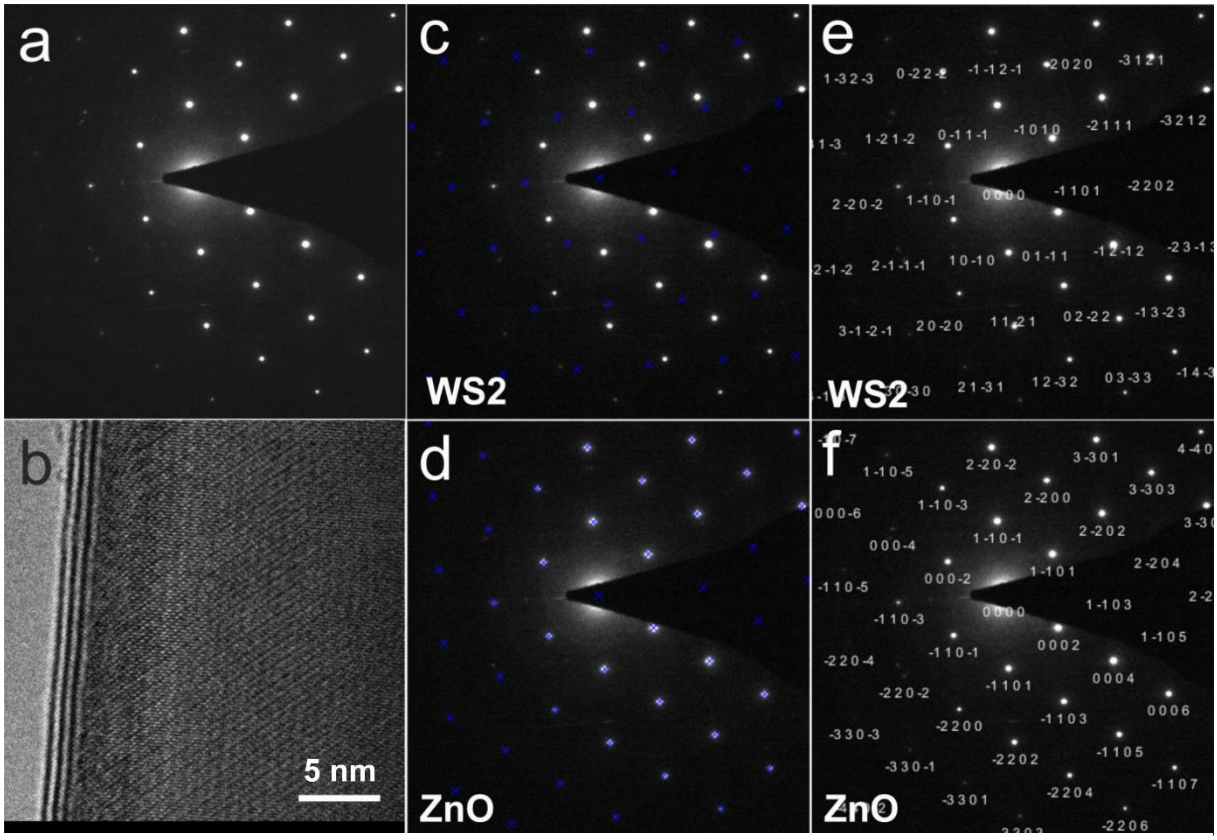

Figure 5.3. SAED analysis of ZnO-WS_2 *core-shell* NWs. (a) SAED pattern, (b) TEM image of the NW, (c-f) phase analysis.

The measured SAED pattern of a ZnO-WS_2 NW is shown in *Fig. 5.3*. Analysis revealed only two distinct phases, WS_2 and ZnO, with high crystallinity. To

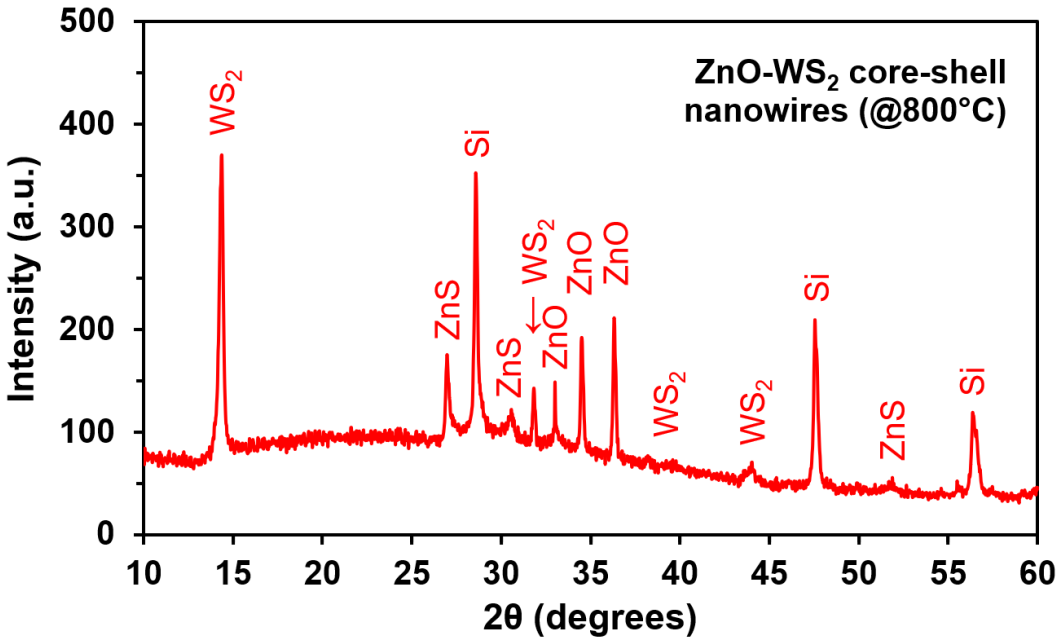

Figure 5.4. XRD pattern of ZnO-WS_2 *core-shell* NW array on Si(100)/SiO_2 substrate.

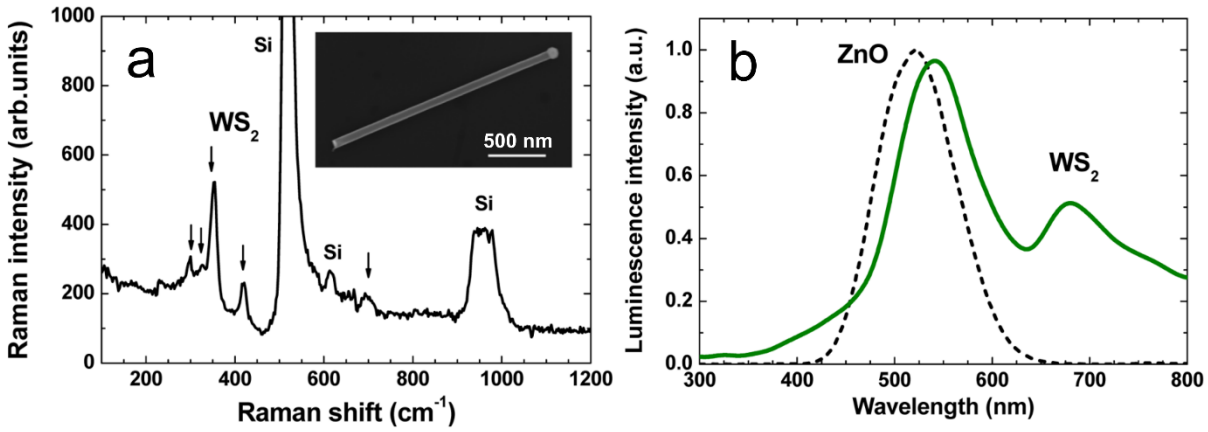

Figure 5.5. (a) Micro-Raman spectrum of a single ZnO-WS_2 *core-shell* NW on Si(100)/SiO_2 substrate (The inset shows a SEM image of the studied NW), (b) room-temperature photoluminescence spectra of pure ZnO NWs (dashed curve) and ZnO-WS_2 *core-shell* NWs (solid curve).

complement the SAED measurement, XRD pattern of the NW array on Si(100)/SiO_2 substrate was also measured (see *Fig. 5.4*). Bragg peaks corresponding to WS_2 (ICDD-PDF #08-0237), ZnO (ICDD-PDF #36-1451), ZnS (ICDD-PDF #36-1450) phases and Si substrate were identified. Although the amount of ZnS in the sample was high enough to be detected by XRD, only a sub-monolayer was present in the ZnO-WS_2 NWs [75].

Micro-Raman spectroscopy was used to support the formation of WS_2 on ZnO NWs. Individual NWs were transferred on top of a clean Si(100)/SiO_2 substrate. *Fig. 5.5(a)* shows room-temperature micro-Raman spectra of a typical ZnO-WS_2 NW (see SEM image in the inset). The two main optical phonon modes $^1E_{2g}$ at 354 cm^{-1} and A_{1g} at 419 cm^{-1} were detected, as well as several other weak Raman bands of WS_2 phase were observed and are indicated with arrows. The positions of the

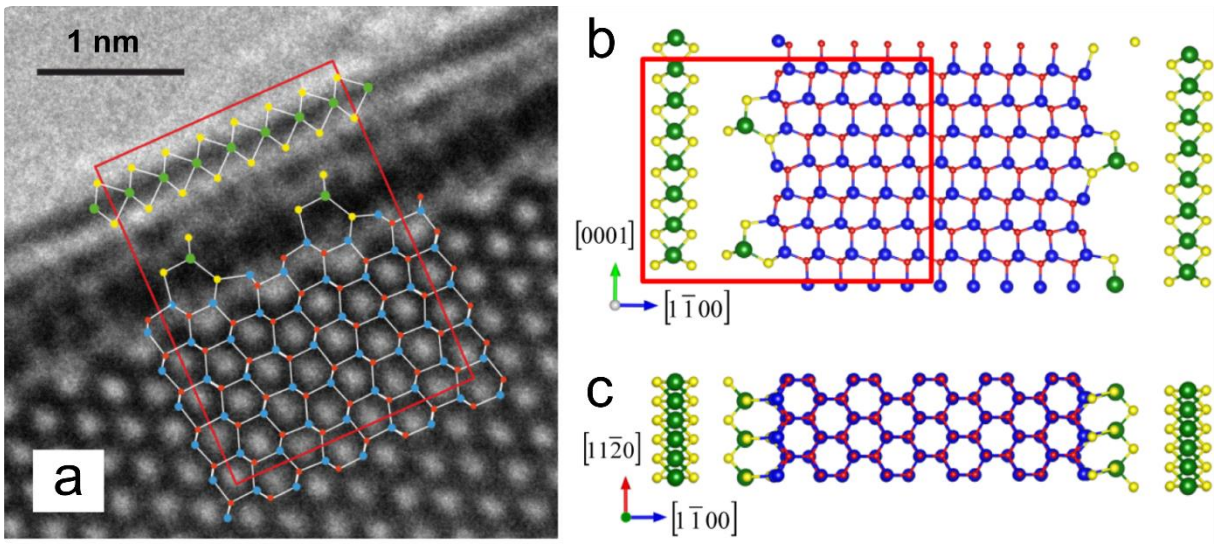

Figure 5.6. (a) Imposition of optimized atomistic model of ZnO(1$\bar{1}$00)/ 0.5 ML WS_2(1$\bar{1}$00)/WS_2(0001) interface on top of the TEM image of ZnO-WS_2 *core-shell* NW and sections of the same interface across (b) (11$\bar{2}$0) and (c) (0001) planes.

measured bands correspond to the values of bulk WS_2 (355.5 and 420.5 cm^{-1}, respectively) [31], however, the intensity ratio between those bands implies that the thickness of the WS_2 shell is close to a monolayer [77]. The large peaks at 521 and 959 cm^{-1} correspond to optical modes of the silicon substrate. No Raman signal was obtained from the ZnO NW core due to its weak intensity when excited at 532 nm.

Room-temperature photoluminescence (PL) spectra of pure ZnO NWs and ZnO-WS_2 NWs are shown in *Fig. 5.5(b)*. Pure ZnO NWs typically exhibit a defect-related PL band at around 520 nm [78], which was observed in our measured spectrum. The PL spectrum of ZnO-WS_2 NWs is more complicated as it contains emission bands from both ZnO and WS_2 phases at around 540 nm and 680 nm, respectively. Here, ZnO-related band red-shifted in comparison to pure ZnO NWs, that may be caused by electron density redistribution, formation of ZnS submonolayer or influence of additional defects. Similarly, red-shift was observed for the WS_2-related band, as PL band of 2D WS_2 microcrystal reference sample is located at 640 nm that corresponds to direct bandgap of 1.9 eV. The shift of the WS_2 PL peak might originate from the influence of the underlaying ZnO NW substrate.

In collaboration with *Laboratory of Computer Modelling of Electronic Structure of Solids* in ISSP UL, large-scale *ab initio* calculations were performed to develop an atomistic model of the ZnO and WS_2 interface. It was experimentally observed that WS_2(0001) shell grew on ZnO(1$\bar{1}$00) NW substrate. Through the theoretical calculations it was found that WS_2(1$\bar{1}$00) submonolayer bridging structures act as pads between the core and the shell for such orientation to be stable (see *Fig. 5.6*). The stability of these submonolayers is higher if their quasimolecular groups are separated by at least a next-neighbour distance, and that reduces the strain of WS_2(0001) shell. This model explains the strong adhesion of the WS_2 layer to ZnO NW and is in agreement with the experimentally estimated interplanar interface distance [75].

5.2 GaN-ReS_2, ZnS-ReS_2 and ZnO-ReS_2 *core-shell* nanowires

ReS_2 exhibits much weaker interlayer coupling in comparison to other 2D materials with the indirect-to-direct bandgap transition in monolayers, therefore, it remains a direct bandgap (E_g ~ 1.5–1.6 eV) semiconductor in bulk, few-layer and monolayer forms [16]. It possesses a unique distorted octahedral (1T) structure resulting in distinct anisotropic optical and electrical properties along in-plane directions [79] that may be useful for emerging applications in electronics (carrier mobility around 30-40 $cm^2V^{-1}s^{-1}$) and optoelectronics [80,81]. 2D ReS_2 has been previously obtained by mechanical exfoliation [81] or variations of CVD: by evaporation different rhenium precursors (Re, ReO_3, Re_2O_7, NH_4ReO_4) [82,83] or by converting pre-deposited metallic Re film [84]. As ReS_2 exhibits strong interlayer decoupling, out-of-plane growth is predominant on many substrates, leading to growth of wrinkled low-quality polycrystalline films or thick flower-like ReS_2 via typical CVD process [83]. In this work, first time growth of few-layer ReS_2 on different semiconductor material NWs (GaN, ZnS, ZnO) was demonstrated. Amorphous non-stoichiometric ReO_x coating was deposited on pure NWs by reactive DC magnetron sputtering, followed by sulfurization of the coating in a quartz tube reactor at 800°C.

SEM images of the as-grown *core-shell* nanostructures (see *Fig. 5.7*) show that the length of NWs is preserved after the procedure and matches their respective pure NWs length before the high-temperature treatment, as well as the density of the NW arrays is maintained. However, a morphology changes of ZnO-ReS_2 NWs upon heating at 800°C can be observed, that indicate an occurrence of a recrystallization process.

TEM was used to study the inner crystalline structure of the NW heterostructures. *Fig. 5.8* shows TEM images of as-grown GaN-ReS_2 (a,b), ZnS-ReS_2 (c,d) and ZnO-ReS_2 (e,f) *core-shell* NWs prepared at 800°C. The lower magnification images show that GaN and ZnS NWs maintain their straight shape,

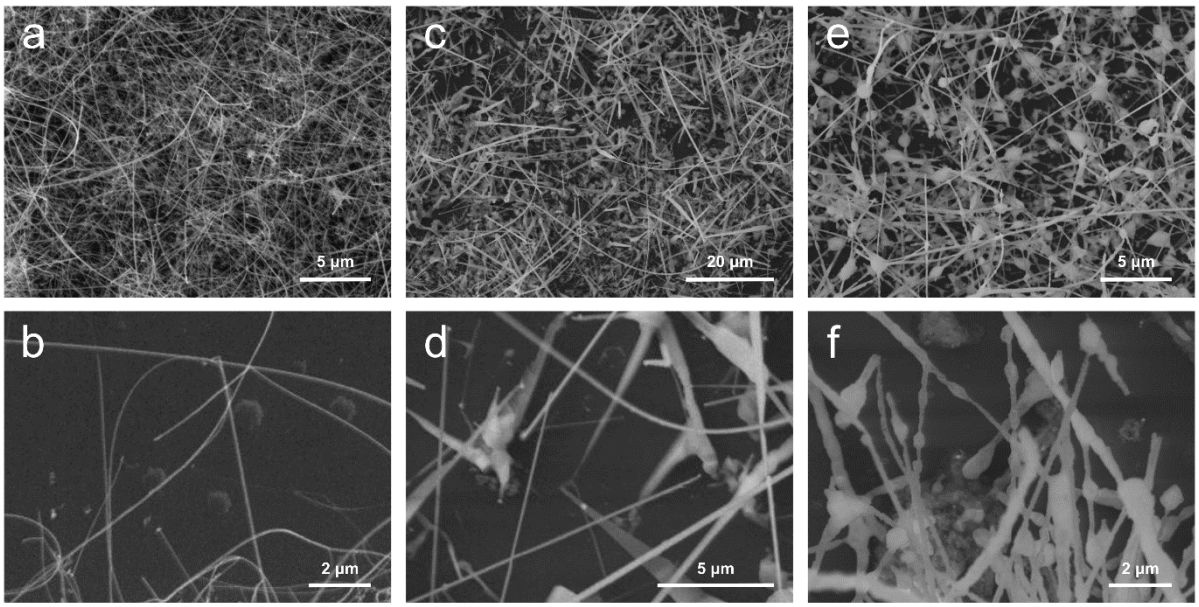

Figure 5.7. SEM images of (a,b) GaN-ReS_2, (c,d) ZnS-ReS_2 and (e,f) ZnO-ReS_2 *core-shell* NWs, prepared at 800°C, at different magnifications.

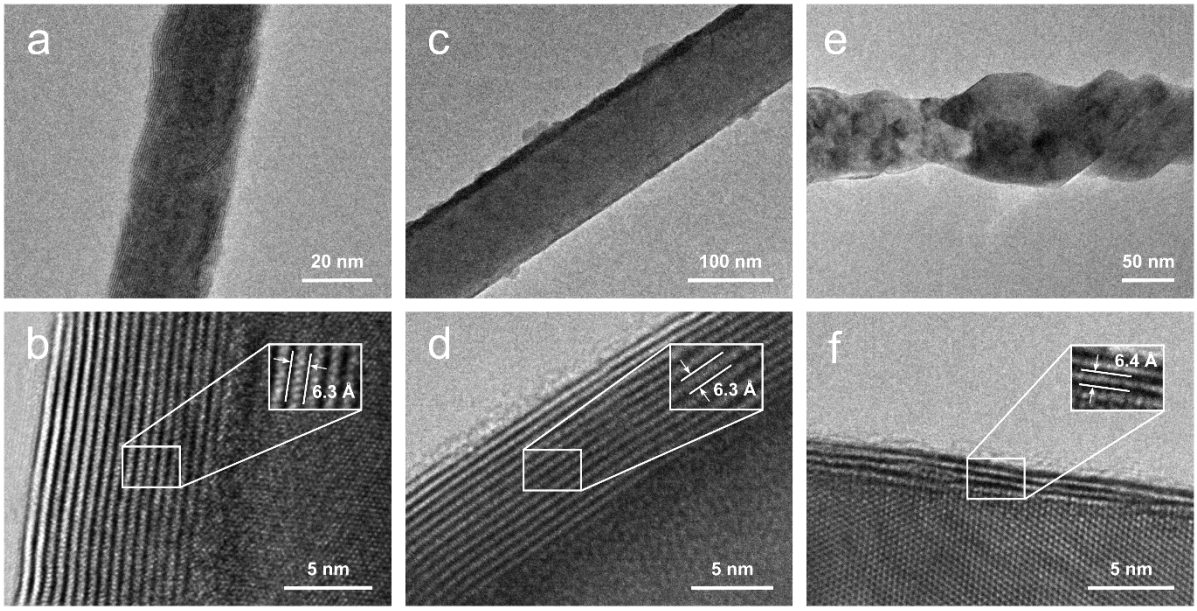

Figure 5.8. TEM images at different magnifications of as-grown (a,b) GaN-ReS_2, (c,d) ZnS-ReS_2, and (e,f) ZnO-ReS_2 *core-shell* NWs, prepared at 800°C. The insets show the measured atomic interlayer distances between ReS_2 layers.

however, ZnO NWs undergo a transition to an irregular shape as was also observed in SEM. The higher magnification TEM images reveal the layered structure of ReS_2 shell (it can be seen as parallel black and white lines along the nanowire surface) with a measured interlayer distance of around 6.3-6.4 Å for all samples, that closely matches the lattice constant a = 6.45 Å of triclinic ReS_2 [85]. The typical thickness of the ReS_2 shell varies from 2-10 monolayers (each consisting of S-Re-S atomic planes), and the shell is uniformly distributed over the length of the NWs with only slight variations of thickness. Furthermore, the single-crystalline nature of the core NWs is visible (in NWs with diameter less than 80 nm) indicating high crystalline quality of the as-prepared *core-shell* heterostructures.

According to TEM measurements, the optimal sulfurization temperature was found to be 750-800°C in order to obtain high-quality single-crystalline ReS_2 layers from the magnetron-sputtered rhenium oxide coating. ReS_2 shell converted at 750°C still exhibited polycrystalline nature indicated by non-parallel placement of the layers while the TEM images in *Fig. 5.8* shows high crystallinity at 800°C. On the other hand, in the case of ZnO NWs, a structural change of the NW can be observed around 750°C, therefore a further study was performed. It was observed that at 700°C the ReS_2 is still polycrystalline, whereas it becomes single-crystalline at higher temperatures, while the ZnO core re-crystallizes at 750°C. Evidently, ZnO NWs undergo a sulfurization process at this temperature and are converted to ZnS phase [86,87]. Worth noting, that no detectable formation of ZnS phase at 800°C was observed in previously discussed ZnO-WS_2 *core-shell* NWs due to the unique growth mechanism of the WS_2 shell [75].

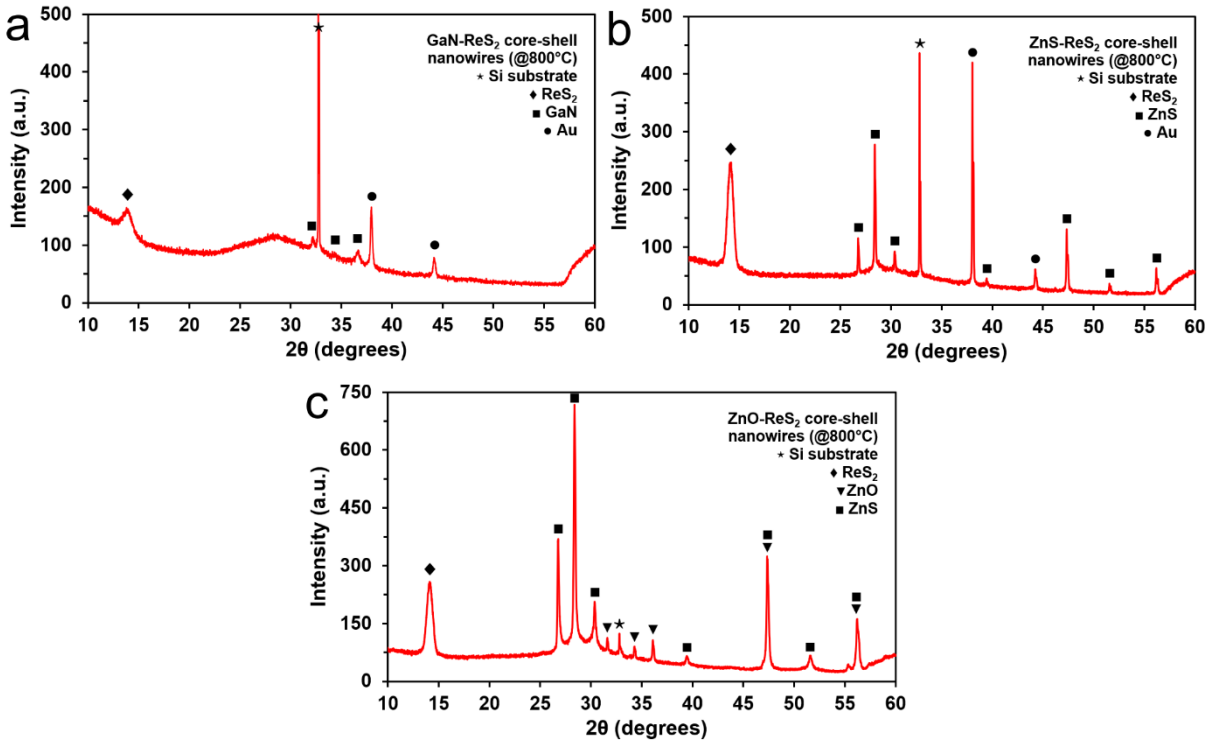

Figure 5.9. XRD patterns of as-grown (a) GaN-ReS_2, (b) ZnS-ReS_2, and (c) ZnO-ReS_2 *core-shell* NW arrays on Si(100)/SiO_2 substrates, prepared at 800°C. Note the ZnS phase peaks in ZnO-ReS_2 pattern that emerges due to a partial or full conversion of ZnO to ZnS which starts at around 750°C.

To confirm the presence of phases in the as-grown *core-shell* NW samples, XRD measurements were performed on the nanowire arrays (converted at 800°C) on Si(100)/SiO_2 substrates (see *Fig. 5.9*). All XRD patterns contain a strong ReS_2 (002) peak of the triclinic phase (ICDD-PDF #52-0818) as well as Bragg peaks attributed to the Si(100) substrate at 33 degress and gold nanoparticles used for VLS growth (ICDD-PDF #04-0784). For GaN-ReS_2 and ZnS-ReS_2 NW samples, GaN (ICDD-PDF #50-0792) and ZnS (ICDD-PDF #36-1450) Bragg peaks are clearly apparent. For ZnO-ReS_2 NWs samples, both ZnO (ICDD-PDF #36-1451) and ZnS phases are present, confirming that ZnO NWs are partly or fully converted to ZnS above 750°C as was observed in TEM measurements. Worth noting, that the ratio between ReS_2 and nanowire XRD peak intensity is related not only to the amount of ReS_2 on the NWs, but also on the Si(100)/SiO_2 substrate, thus it cannot be properly used to quantitatively describe the phase composition ratio of the *core-shell* heterostructures. As the ZnO NWs undergo sulfurization process before single-crystalline ReS_2 shell is formed, such material might not be suitable template for ReS_2 growth, whilst it was possible to grow high-quality single-crystalline layers of ReS_2 on GaN and ZnS NWs.

To confirm the presence of ReS_2, micro-Raman scattering spectra of as-grown ZnO-ReS_2, ZnS-ReS_2 and GaN-ReS_2 *core-shell* NWs (measured in each case from a single NW) are compared to that of bulk ReS_2 in *Fig. 5.10*. ReS_2 Raman active modes are indicated by the vertical lines. All the Raman active phonon modes were observed in bulk ReS_2 and *core-shell* NWs. The Raman bands are narrower for bulk ReS_2 and GaN-ReS_2 NW, whereas they are slightly broadened for ZnO-ReS_2 and ZnS-ReS_2

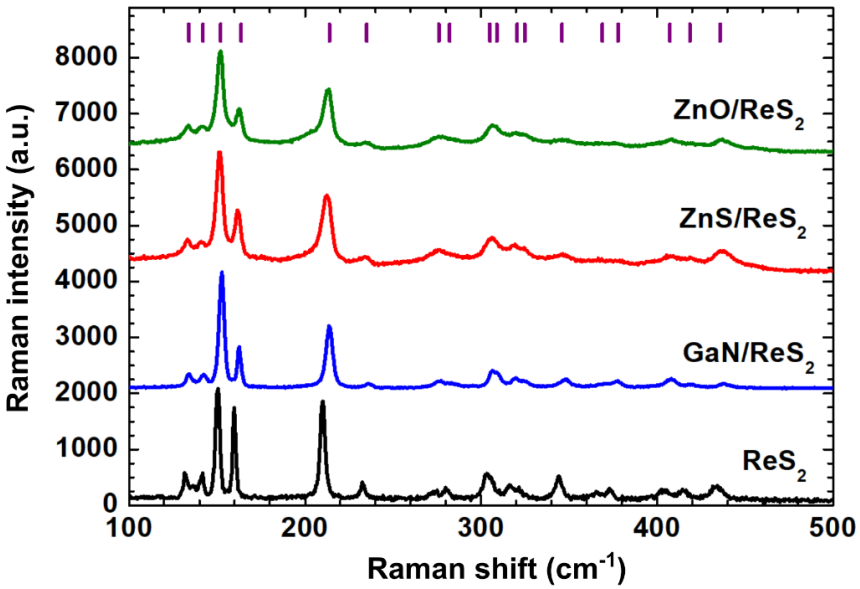

Figure 5.10. Micro-Raman spectra of ZnO-ReS_2, ZnS-ReS_2 and GaN-ReS_2 *core-shell* NWs, prepared at 800°C, and bulk ReS_2. Vertical lines indicate the positions of the Raman active A_g phonon modes.

NWs. The broadening leads to an overlap of nearest bands located around 280 cm^{-1}, 307 cm^{-1} and 322 cm^{-1}. The most intense bands (E_g-like modes) are located at about 152 cm^{-1}, 163 cm^{-1} and 213 cm^{-1} and mainly involve in-plane vibrations of Re atoms [88].

5.3 ZnO-MoS_2 *core-shell* nanowires

MoS_2 might be the most popular and well-studied 2D TMD [8]. Bulk MoS_2 has a 1.2 eV indirect bandgap while its monolayer has a direct bandgap of 1.8 eV [12]. It has relatively good mobility (~700 $cm^2V^{-1}s^{-1}$), therefore, it has been widely studied for applications in electronics and optoelectronics. 2D monolayer MoS_2 has been obtained using quite a few different methods, most relevant to this work being CVD, conversion of MoO_3 and thermal decomposition of $(NH_4)MoS_4$ [26]. In this work, first time synthesis of ZnO-MoS_2 *core-shell* NWs, where ZnS interlayer is formed between ZnO and MoS_2, was demonstrated [86]. The process involves immersion of pure ZnO NWs in ammonium heptamolybdate tetrahydrate solution followed by annealing in sulfur atmosphere at 700°C.

SEM was used to tune the NW growth process and to observe the morphology change after MoS_2 shell growth. It is clearly visible in *Fig. 5.11(a,b)* that the smooth surface of ZnO NWs immersed in the ammonium heptamolybdate solution becomes significantly more rough and altered (see *Fig. 5.11(c,d)*) after annealing. The NW length is maintained after the heat treatment. Strong electrical charging was observed for the *core-shell* NWs, however was absent for pure ZnO NWs. This may indicate that electrical properties of ZnO NWs were strongly affected by a shell layer, making them less conductive. It is known that sulfur reacts with ZnO at temperatures above 400°C resulting in a formation of ZnS phase [87], which has the value of the bandgap (3.7 eV) larger than ZnO (3.4 eV).

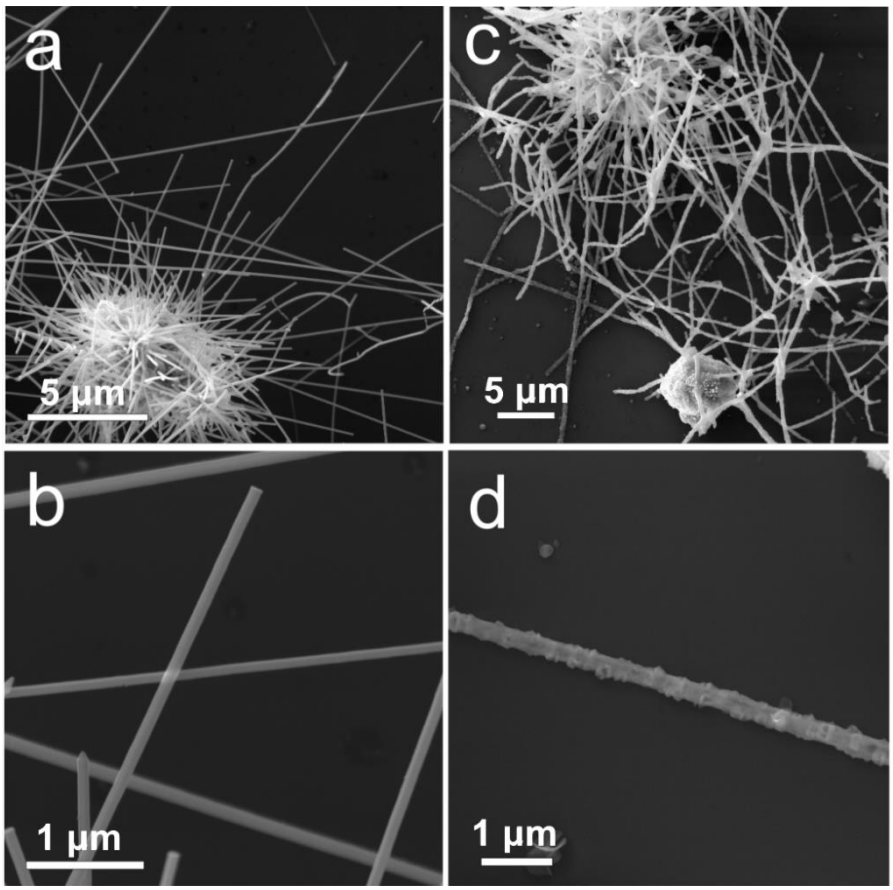

Figure 5.11. SEM images of (a,b) ZnO NWs, immersed in ammonium heptamolybdate solution and dried; (c,d) ZnO-MoS_2 *core-shell* NWs after annealing in sulfur atmosphere at 700°C.

TEM images of *core-shell* NWs annealed in sulfur atmosphere at 500°C and 700°C are shown in *Fig. 5.12*. Sample annealed at 500°C has a polycrystalline shell with some remaining amorphous phase. No MoS_2 shell was found around the NW, however, few crystallites appearing as parallel black lines (*Fig. 5.12(c)*) may be identified as MoS_2. The shell in the sample annealed at 700°C is non-homogeneous and appears as a mosaic of dark and bright spots (*Fig. 5.12(d,e)*) or as microcrystals formed around the NW core (*Fig. 5.12(g,h)*). According to interplanar distance measurements, microcrystals on NW surface can be attributed to zincblende ZnS phase with the interplanar distance d=3.1-3.2 Å (ICDD-PDF #36-1450). It is known that ZnO reacts with sulfur and forms ZnS starting from 400°C. Due to the lattice mismatch and different crystal structure of ZnO core and ZnS shell, the upper layer cannot grow as a smooth single crystal layer on top of ZnO NW surface. Furthermore, NWs prepared at 700°C are coated by few layers of MoS_2, which appears as a number of parallel black lines (*Fig. 5.12(f,i)*). The number of MoS_2 layers varies in the range of 1-8 monolayers, which is probably related to nonhomogeneous coating by ammonium molybdate precursor. The measured distance between monolayers is about 6.25 Å, which corresponds well to 6.2-6.3 Å interlayer distance in MoS_2 (ICDD-PDF #37-1492).

SAED analysis of the *core-shell* NW (see *Fig. 5.13*) revealed the following phases: ZnO zincite (zone axis <0001>), ZnS zincblende (zone axis <001>), and MoS_2 molybdenite phases (zone axis <-2201> and <14-53>). Dominating (the most

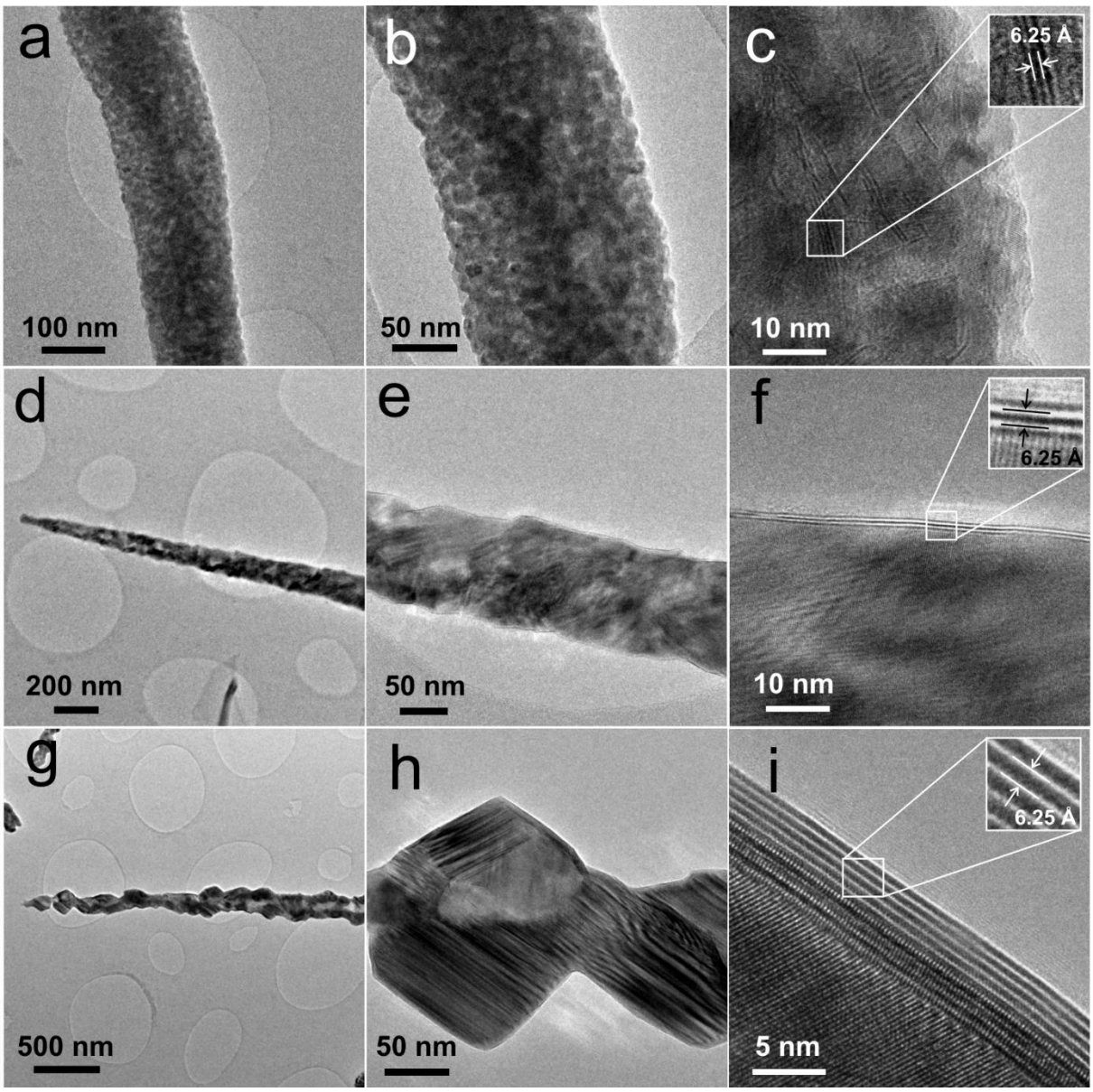

Figure 5.12. TEM images at different magnifications of ZnO-MoS_2 *core-shell* NWs, prepared at (a-c) 500°C and (d-i) 700°C. The insets show the measured atomic interlayer distances between MoS_2 layers.

intensive) diffraction spots belong to the ZnO core, while less intensive to ZnS and MoS_2 phases. Symmetric orientation of MoS_2 reflexes relative to ZnO reflexes may indicate epitaxial growth of MoS_2.

Micro-Raman spectroscopy was used to confirm the formation of MoS_2 layers on the NWs. The in-plane E^1_{2g} mode at 384 cm^{-1} and the out-of-plane A_{1g} mode at 407 cm^{-1} were clearly resolved on the *core-shell* NW (see *Fig. 5.14*) that corresponds to typical MoS_2 Raman spectra [89]. Note that the large peak at ~521 cm^{-1} is the first order of optical mode at k=0 of the underlying silicon substrate.

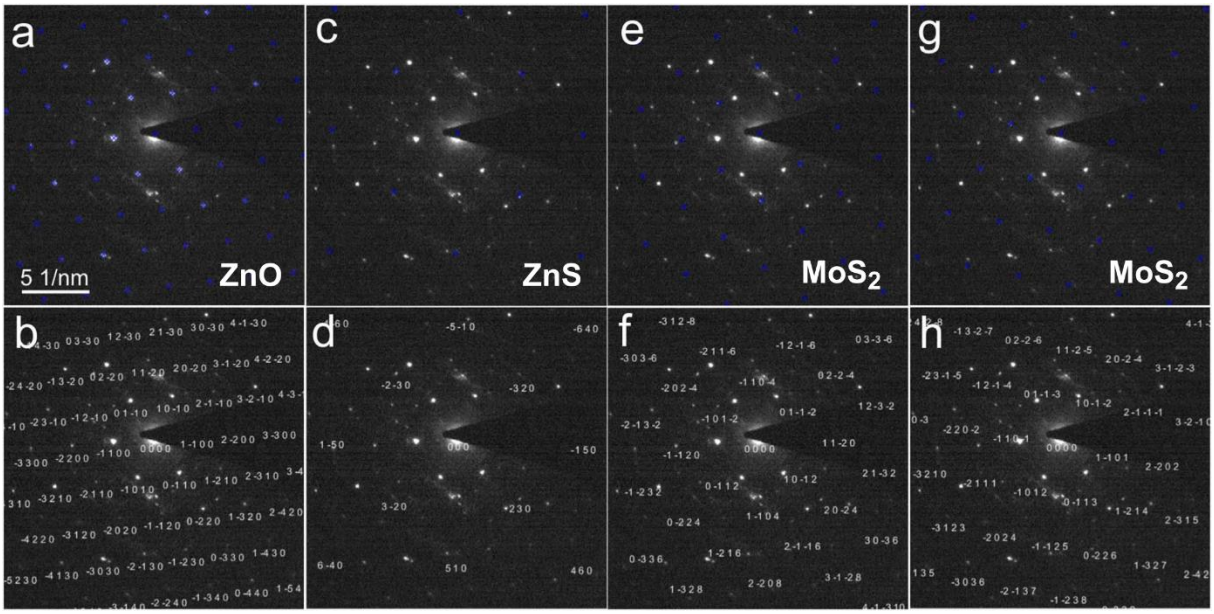

Figure 5.13. SAED analysis of ZnO-MoS_2 *core-shell* NWs. The presence of (a,b) ZnO zincite zone axis ⟨0001⟩, (c,d) ZnS zincblende zone axis ⟨001⟩, MoS_2 molybdenite phases of (e,f) zone axis ⟨−2201⟩ and (g, h) zone axis ⟨14–53⟩ were identified.

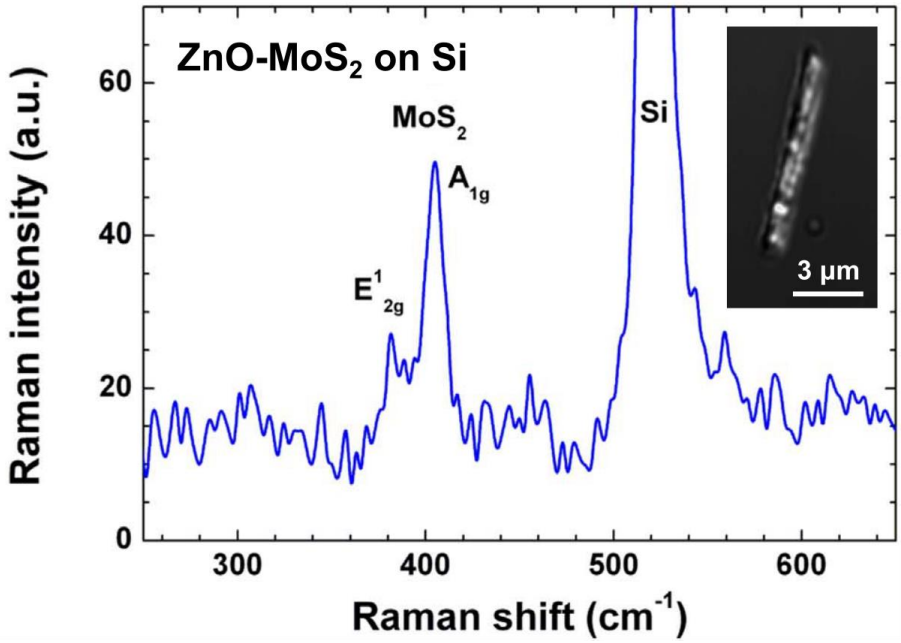

Figure 5.14. Micro-Raman spectra of ZnO-MoS_2 *core-shell* NW on Si(100)/SiO_2 substrate. The inset shows a confocal microscope image of the studied NW.

Alternatively, MoO_3 sacrificial layer was deposited on pure ZnO NWs by reactive DC magnetron sputtering, similar to ZnO-WS_2 *core-shell* NW preparation method discussed previously. After sulfurization of ZnO-MoO_3 NWs at 700°C, morphology of thus obtained *core-shell* NWs is rather similar to the ones produced by immersion in ammonium heptamolybdate solution (see SEM images in *Fig. 5.15(a,b)*). However, MoS_2 shell is usually significantly thicker due to the large amount of deposited MoO_3 precursor (it is difficult to deposit very thin layer of MoO_3

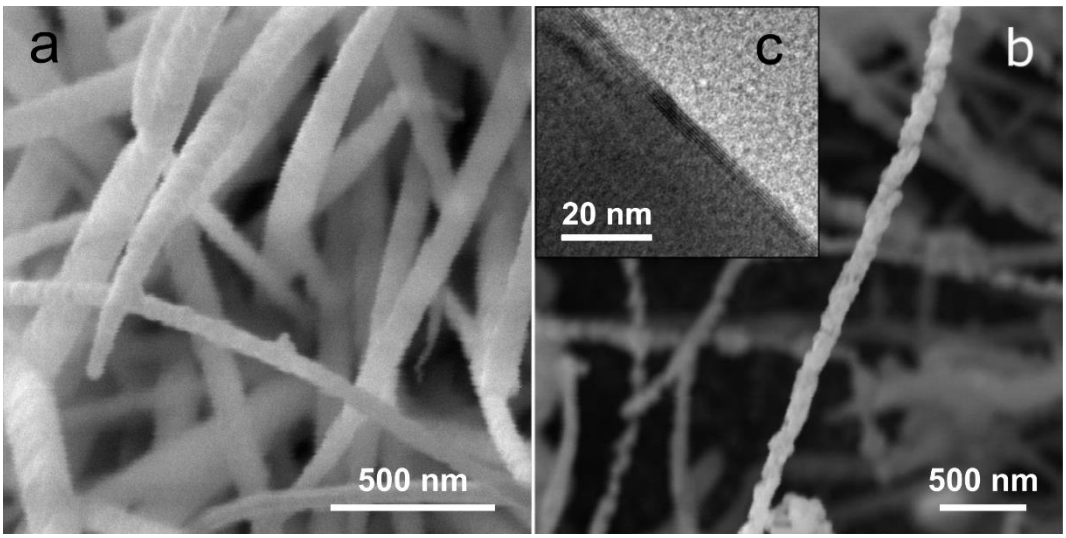

Figure 5.15. SEM images of (a) ZnO-MoO_3 *core-shell* NWs, where the shell has been deposited by magnetron sputtering, (b) ZnO-MoS_2 *core-shell* NWs after annealing in sulfur atmosphere at 700°C. (c) TEM image of the as-prepared *core-shell* NW.

by magnetron sputtering), therefore, the immersion method of molybdenum precursor deposition is more preferable in this case compared to the magnetron sputtering. Nevertheless, TEM image (see *Fig. 5.15(c)*) shows that it is still a viable method how to obtain few-layer MoS_2 on NWs but with less uniformity.

5.4 PbI_2-decorated ZnO nanowires

PbI_2 is a layered vdW material with a similar structure and physical properties as TMDs, however, it is not a TMD but has iodine atoms instead of chalcogens. It is a semiconductor material with a direct 2.2–2.55 eV bandgap and can be used as a photodetector or as an X-ray and γ-ray detector material [90,91]. There are theoretical and experimental studies that show band structure shift from direct bandgap to indirect bandgap when the PbI_2 thickness is reduced from bulk to monolayer [14], as opposed to other more commonly studied vdW materials. Therefore, monolayer PbI_2 is not expected to be an efficient material for optoelectronics applications. Few-layer PbI_2 flakes can be synthesised in a liquid phase [92] or via CVD process [90,93]. In this work, a novel two-step growth process for uniform crystalline PbI_2 nanosheets via reactive magnetron deposition of a lead oxide film followed by subsequent iodination at 420°C to PbI_2 on a ZnO NW substrate was demonstrated, and as-grown hybrid nanostructures were compared with ones prepared via thermal evaporation method [94]. Few-layer PbI_2 did not uniformly cover all surface of NWs, therefore, such heterostructures are not called *core-shell* NWs but PbI_2-decorated NWs instead.

SEM was used to image as-grown individual NWs and NW arrays and study their morphology. Pure ZnO NWs are typically 20–30 μm long with a diameter around 100 nm and exhibit a smooth surface. *Fig. 5.16(a,b)* shows ZnO NWs with a thermally deposited PbI_2 coating. No significant change in diameter is observed; however, a very fine increase in surface roughness is visible. NWs with a sputter-

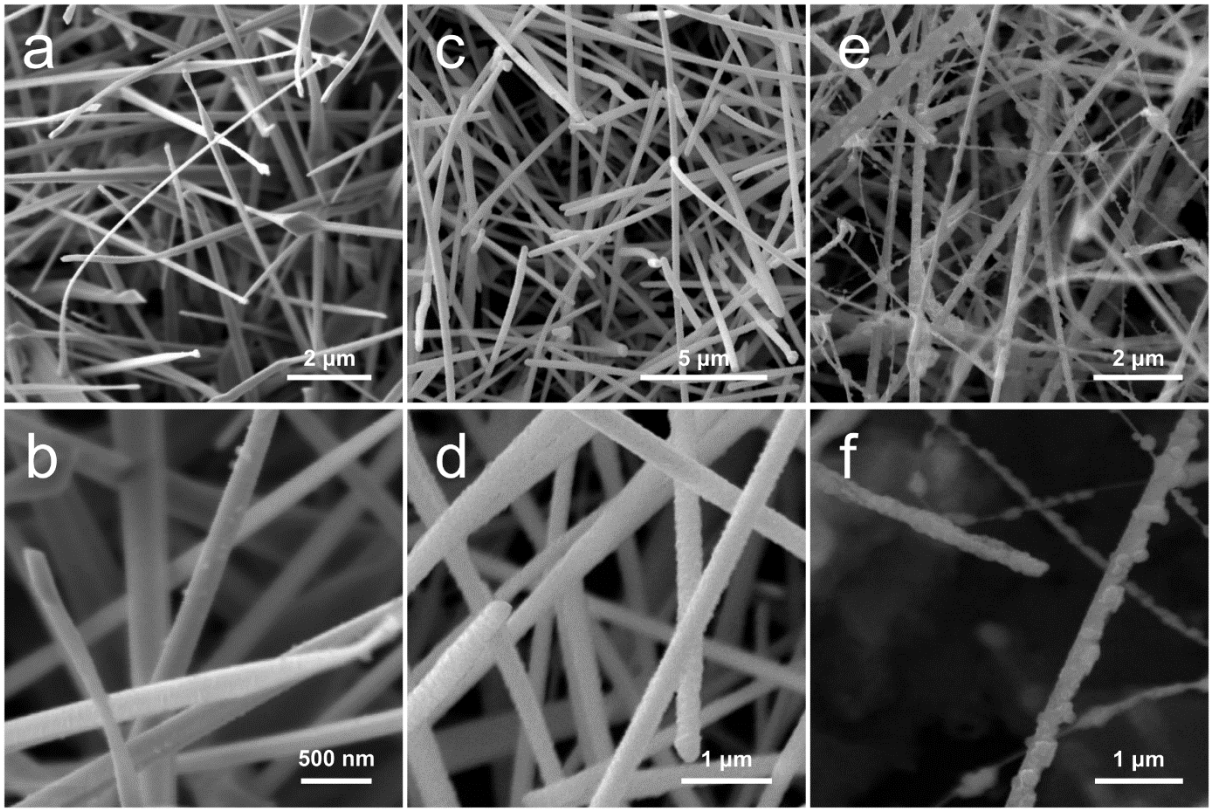

Figure 5.16. SEM images of images of (a,b) ZnO-PbI_2 NWs made by using the thermal evaporation approach; (c,d) ZnO NWs covered by lead oxide deposited by magnetron sputtering; (e,f) ZnO-PbI_2 NWs made by converting the lead oxide coating.

deposited lead oxide coating with a fine roughness are shown in *Fig. 5.16(c,d)*, where a considerable (up to 100 nm) increase in diameter can be seen. After annealing such NWs in iodine vapour at elevated temperatures, the surface roughness greatly increased; however the diameter is significantly reduced as a fraction of the coated material is sublimated after the transformation (see *Fig. 5.16(e,f)*). The final coating is not uniform over the entire length of NWs as some thicker particles and islands can be observed.

A deeper insight into the nanostructures' inner structure was obtained using TEM. *Fig. 5.17(a–c)* shows TEM images of ZnO-PbI_2 NWs obtained by the thermal evaporation method at different magnifications. The lower resolution images show noticeable contrast between the two NW sides (PbI_2 layers correspond to the darker region), indicating non-uniform coating deposition, which is expected from the thermal evaporation approach since it is a line-of-sight method. At a high resolution, the crystalline structure of the nanostructure is revealed. The layers of PbI_2 grown on the ZnO NW surface are distinguishable as parallel black lines. Typically, the thickness of the coating varies between 5–10 monolayers (each consisting of I-Pb-I atomic planes), with interlayer distance measured around 7 Å, which is in a good agreement with the lattice constant (a = 6.979 Å) of bulk hexagonal PbI_2 (ICDD-PDF #07-0235). Furthermore, the single-crystalline nature of the ZnO NWs is clearly visible; the measured interplanar distance is 2.8 Å, corresponding to hexagonal ZnO wurtzite (ICDD-PDF #36-1451). The TEM images of the ZnO-PbI_2 nanostructures

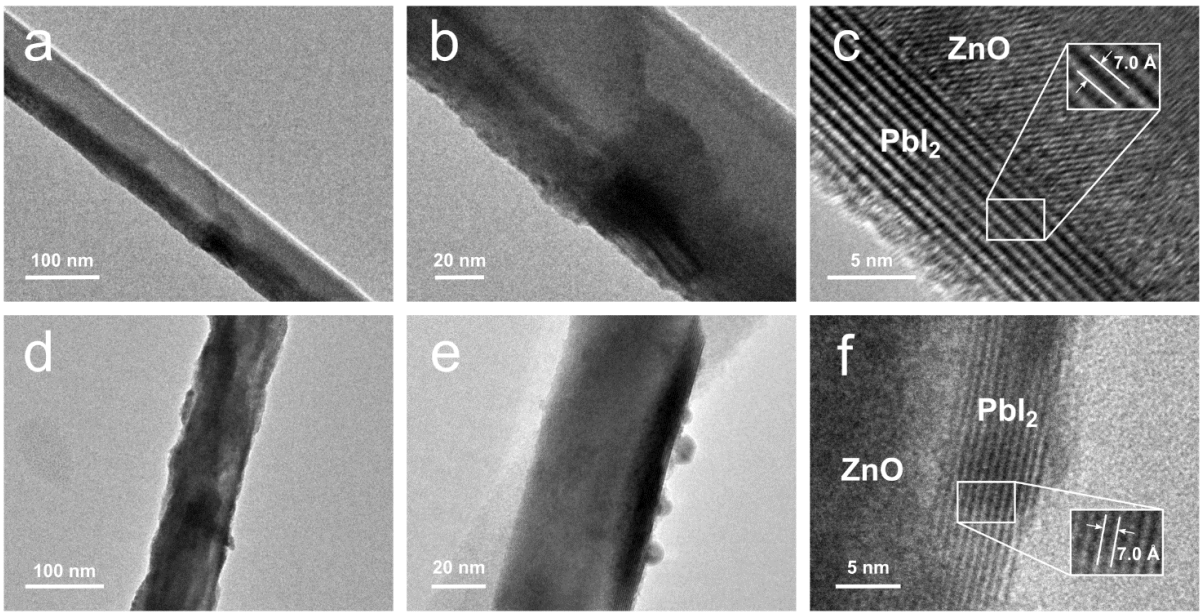

Figure 5.17. TEM images at different magnifications of (a-c) ZnO-PbI_2 NWs made by using the thermal evaporation approach, and (d-f) ZnO-PbI_2 NWs made by converting the magnetron-sputtered lead oxide coating. The insets show the measured atomic interlayer distances between PbI_2 layers.

obtained by conversion of sputter-deposited lead oxide coating are shown in *Fig. 5.17(d–f)*. In this case, the PbI_2 coating is uniformly distributed over the entire ZnO NW surface; however, the surface roughness is significantly increased. The thickness of the coating typically varies between 5–15 monolayers, with some islands being even thicker. As in the first approach, the measured interlayer distance is around 7 Å.

To complement TEM structural investigations and confirm the presence of phases, XRD measurements were performed on the as-prepared samples. *Fig. 5.18* shows XRD patterns of NW arrays prepared by the two approaches: thermal evaporation and converting the magnetron-sputtered lead oxide coating,

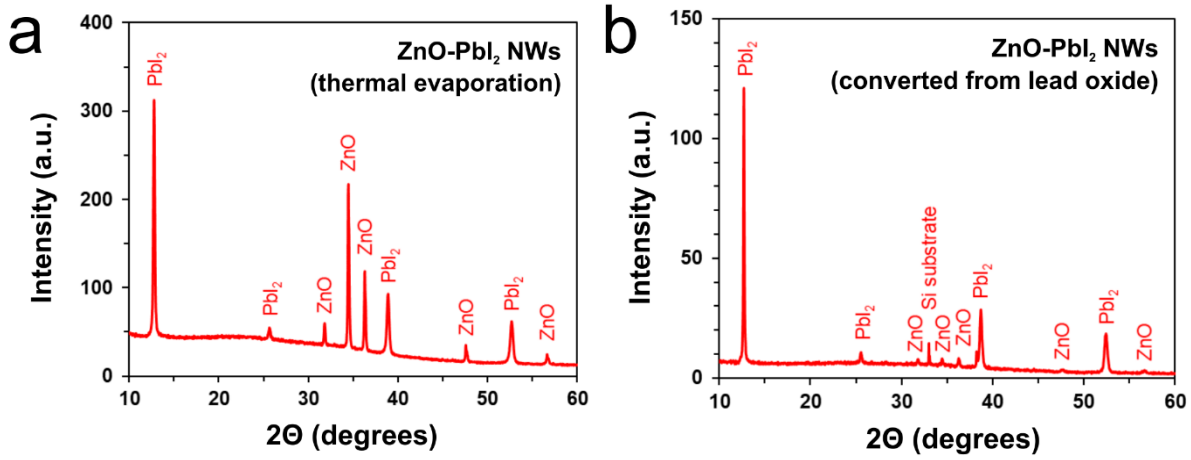

Figure 5.18. XRD patterns of (a) ZnO-PbI_2 NW arrays on Si(100)/SiO_2 substrate made by using the thermal evaporation approach; (b) ZnO-PbI_2 NW arrays on Si(100)/SiO_2 substrate made by converting the magnetron-sputtered lead oxide coating.

respectively. Both patterns indicate highly crystalline hexagonal ZnO wurtzite (ICDD-PDF #36-1451) and hexagonal PbI_2 (ICDD-PDF #07-0235) phases. No other phases were observed, confirming the high crystallinity of the as-prepared nanostructures, as did the TEM investigations. It is worth noting that the ratio between PbI_2 and ZnO peak intensity is not only related to the amount of PbI_2 on ZnO NWs but also the amount of PbI_2 crystallites on the Si/SiO_2 substrate. Therefore, spectra cannot be properly used to describe the phase composition ratio in the nanostructures. Furthermore, ZnO NW Bragg peak intensities vary between the samples - due to an inhomogeneous gold nanoparticle catalyst deposition from colloid on the silicon substrate; the density of as-grown ZnO nanowires arrays was also not homogeneous while the PbI_2 layer is relatively homogeneous over the substrate due to the precisely controllable deposition method. In *Fig. 5.18(b)*, the Bragg peak at 33° is attributed to diffraction in the Si(100) substrate (forbidden Si(200) reflection).

To study the optical properties, room temperature PL in the as-prepared samples was measured in a wavelength range from 400 to 650 nm, excited by a 266 nm laser. Generally, PbI_2 has a direct band-to-band transition at around 495 nm (~2.5 eV) [95]; however, a broad band peaked at 510–525 nm has been previously observed and attributed to recombination through defects, such as iodine and lead vacancies [90]. The PL spectrum of pure ZnO NWs exhibits a defect-related band at ~520 nm [78]. Therefore, the interpretation of the ZnO-PbI_2 nanostructure spectra might be ambiguous due to this ZnO and PbI_2 PL band overlapping, since higher ZnO PL intensities might lead to indistinguishable PbI_2 PL peaks or vice versa. *Fig. 5.19* depicts the measured PL spectra of pure ZnO NWs, the PbI_2 thin film reference sample, and the ZnO-PbI_2 nanostructures prepared via both approaches. It is worth noting that the PL intensity is depicted in arbitrary units and does not contain information about the relative intensities between the obtained spectra. The ZnO NW

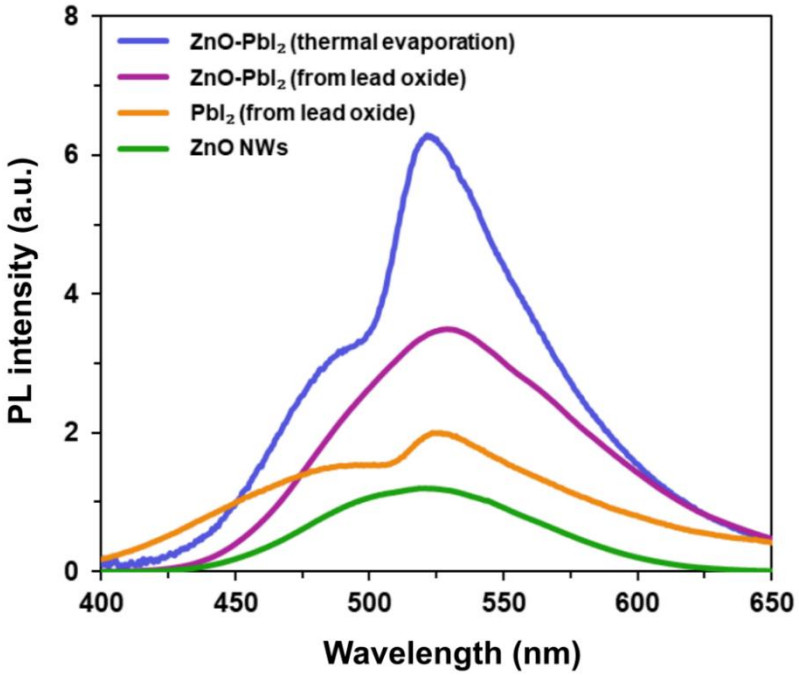

Figure 5.19. Room-temperature photoluminescence spectra at the excitation wavelength of 266 nm of the different as-prepared samples.

spectrum exhibits the typical defect band at 520 nm and the PbI_2 thin film sample (prepared by converting lead oxide film) shows two emission peaks: the direct band-to-band transition at around 495 nm and the defect-related band at around 530 nm. The ZnO-PbI_2 nanostructures (prepared by thermal evaporation approach) exhibit two peaks at 495 nm and 525 nm; however, the nanostructures prepared via lead oxide conversion exhibit only one band with a peak at 530 nm due to the higher intensity overlapping ZnO peak. One can see and interpret the difference between the PbI_2 peak ratio for samples prepared with different methods due to the defect-related peak maximum shift. For example, the defect/band-to-band peak intensity ratio for thermally evaporated PbI_2 is ~2, while for lead oxide converted PbI_2, it is ~1.33. Therefore, by also considering the ZnO peak contribution, one can qualitatively assume that lead oxide conversion via iodination leads to fewer defects in PbI_2 coatings than the thermal evaporation approach.

5.5 Single nanowire photodetectors

To investigate the applicability of the developed NW heterostructures in optoelectronics, two-terminal single-NW photodetector devices were fabricated for the most perspective nanostructures. The selection was based on the structural and composition studies. The device fabrication and characterization procedures were previously described in *Chapters 4.5* and *4.6*. A typical as-fabricated device is shown in *Fig. 5.20*, where a single NW is placed between gold microelectrodes. At least five single-NW photodetectors for each material or synthesis method were fabricated so that consistent conclusions could be made.

To characterize such devices, dark state I_{ds}-V_{ds} curves, dark current, current enhancement ratio I_{on}/I_{off}, rise and decay photoresponse time, spectral responsivity R_λ and external quantum efficiency EQE were determined; devices were measured at 405, 532 and 660 nm wavelength light illumination and usually at 1V bias voltage. Stability and reversibility of on-off measurements was also evaluated. Rise and decay time of NW devices is defined as the required time for the photocurrent to increase or decrease to 90% or 10% of its maximum value, respectively. R_λ and EQE are used to evaluate photoconductive properties of a material - R_λ and EQE are respectively defined as $R_\lambda = \Delta I/(PS)$ and $EQE = hcR_\lambda/(e\lambda)$, where ΔI is the difference between the

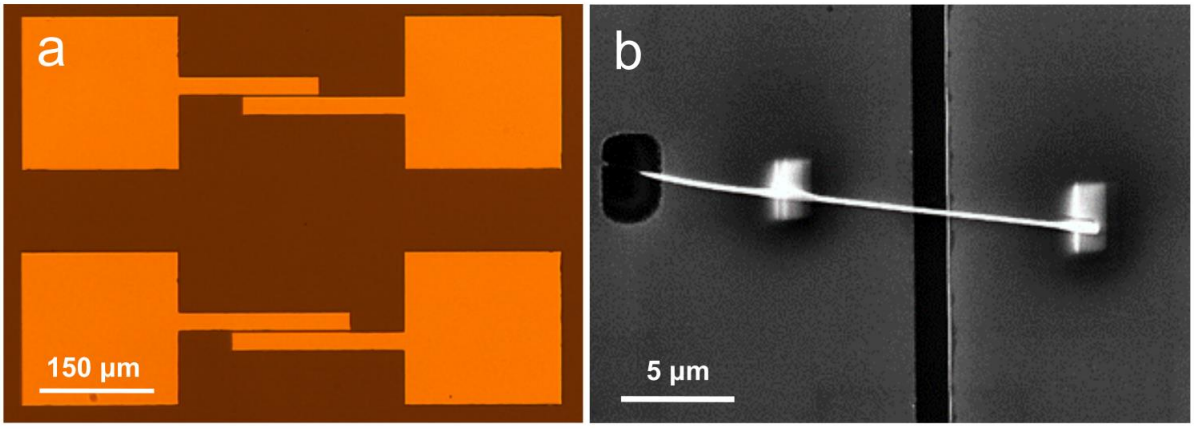

Figure 5.20. (a) Optical microscope image of gold microelectrodes on an oxidized silicon substrate; (b) SEM image of a typical as-prepared nanowire photoresistor.

photocurrent I_{on} and the dark current I_{off}, *P* is the light power density, *S* is the effective illumination area (estimated as the NW length between contacts × NW diameter), *h* is Planck's constant, *c* is the speed of light, *e* is the electron charge and λ is the light wavelength. Large R_λ and EQE values correspond to high photodetector sensitivity, and EQE larger than 1 means there is a photoconductive gain in the device.

5.5.1 PbS, In_2S_3, CdS and ZnSe nanowire photodetectors

Firstly, the method of single-NW device fabrication and characterization was developed and tested on pure metal chalcogenide NWs [96]. A study of such pure NW devices is necessary in order to better understand the photoelectric behaviour of more complicated *core-shell* systems afterwards.

Fig. 5.21 shows the measured I_{ds}-V_{ds} curves of different as-prepared NW devices. Typically, nearly symmetrical characteristics were obtained for all investigated NW materials, therefore, indicating that ohmic contacts were formed between the electrodes and the NW. Features of non-linear quadratic ($I \sim V^2$) behaviour of the I-V curves may be interpreted as an effect of the space-charge limited current (SCLC), as other groups have previously shown in different material nanowires [97,98]. In addition, it is worth noting that as-fabricated devices exhibit high resistance, wherein, most probably a considerable part arises due to the contacts. Possible causes of such increased resistance include high resistance of deposited Pt contacts due to a carbon presence from the metal-organic precursor [99].

Next, as-prepared NW device electrical response to an illumination of a light at different wavelengths was investigated. On-off photoresponse measurements, which are based on photoinduced conductivity changes, for three different

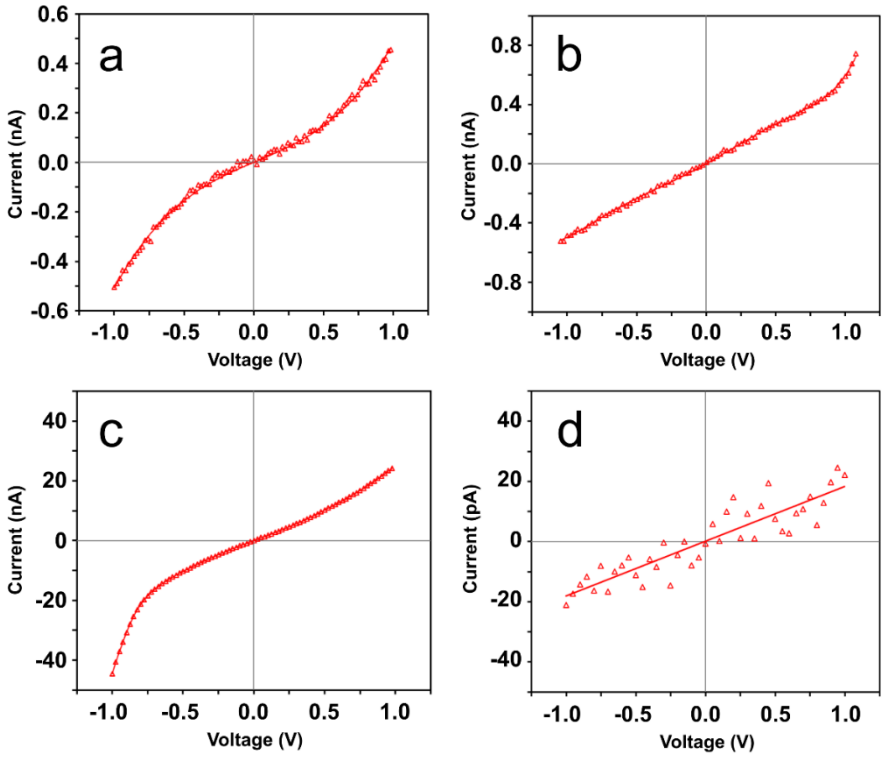

Figure 5.21. Dark-state I_{ds}-V_{ds} characteristics of (a) PbS, (b) In_2S_3, (c) CdS and (d) ZnSe NW photodetectors.

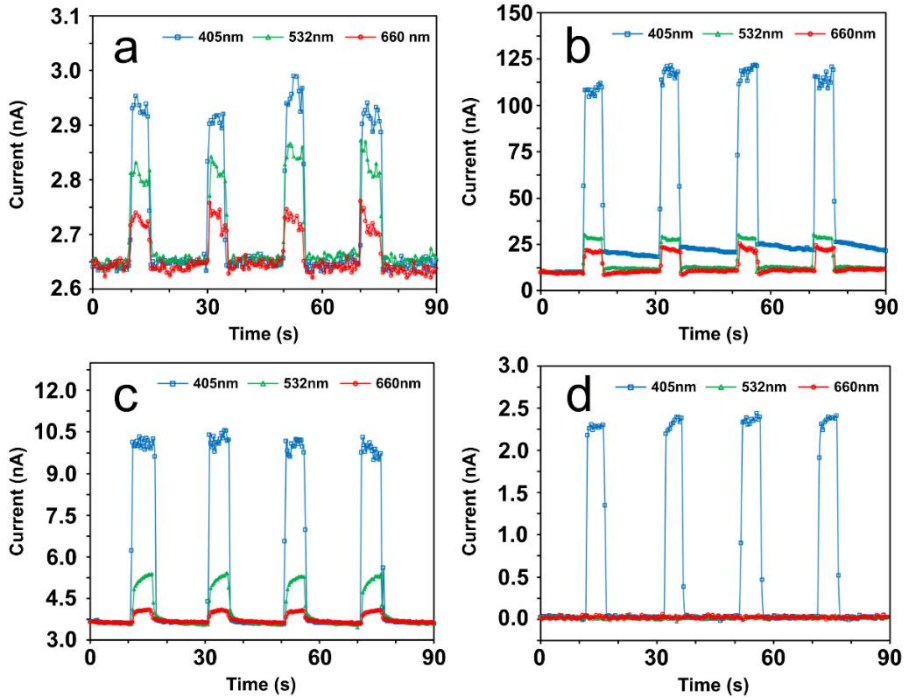

Figure 5.22. On-off photoresponse measurements of (a) PbS, (b) In_2S_3, (c) CdS and (d) ZnSe NW photodetectors at V_{ds} = 1 V bias voltage and 0.5 W/cm^2 light intensity of 405 nm, 532 nm and 660 nm wavelength light illumination.

illumination wavelengths at V_{ds}=1V bias of as-prepared NW photodetector devices are depicted in *Fig. 5.22*. It can be seen that all four studied NW materials exhibit rapid (< 1 second, in most cases) increase and decrease of the current after the illumination is turned on or off, respectively, except in the case of the In_2S_3 NW current decay time for 405 nm illumination, which features a second, slower time component, most probably do to a presence of trapping centres.

Table 5.1 shows the comparison of current enhancement ratios (I_{on}/I_{off}) of the studied NW materials in the context of their respective bandgap, which determines their cut-off wavelengths. Firstly, it can be seen that PbS NWs exhibit weak (I_{on}/I_{off} close to 1) photoresponse to all three illumination wavelengths; however, linear ratio vs. wavelength dependence was observed. Secondly, In_2S_3 and CdS NWs exhibit strong photoresponse to 405 nm illumination, and significantly weaker one to 532 nm and 660 nm illumination. Finally, ZnSe NWs show very strong response to 405 nm light, and no photoresponse was observed while illuminating them with 532 nm

Table 5.1. Comparison of the photoresponses of the studied single-nanowire photodetectors.

Materials	**E_g (eV)**	**I_{dark} at 1V (nA)**	**I_{on}/I_{off} ratio**		
			at 405 nm (3.06 eV)	**at 532 nm (2.33 eV)**	**at 660 nm (1.88 eV)**
PbS NW	0.41	2.65	1.11	1.07	1.03
In_2S_3 NW	2.1	9.95	11.3	2.8	2.1
CdS NW	2.4	3.65	2.7	1.4	1.1
ZnSe NW	2.7	0.02	115	1	1

and 660 nm wavelength light. Obtained I_{on}/I_{off} value tendencies, for the most part, are as was anticipated from the material bandgap values; however, relatively weaker photoresponse to 660 nm illumination was expected for either CdS or In_2S_3 NWs. Such above-cut-off-wavelength photosensitivity may be caused by defects, like impurity doping or surface states. *Table 5.2* contains the calculated R_λ and EQE values of the studied NW devices. The obtained data shows a relatively wide range of values for different NW materials, however, these values are comparable to other typical *state-of-art* 1D nanostructure photodetector [100], thus indicating the potential to use such materials in future applications.

Table 5.2. Responsivity R_λ and external quantum efficiency EQE values of the studied single-nanowire photodetectors at different illumination wavelengths.

Materials	Responsivity R_λ, A/W			EQE		
	at 405 nm	at 532 nm	at 660 nm	at 405 nm	at 532 nm	at 660 nm
PbS NW	0.06	0.04	0.02	18%	9%	3%
In_2S_3 NW	16.01	2.80	1.71	4903%	652%	321%
CdS NW	0.86	0.20	0.05	264%	47%	10%
ZnSe NW	0.20	0	0	62%	0	0

5.5.2 ZnO-WS_2 *core-shell* nanowire photodetectors

ZnO-WS_2 *core-shell* NW photoelectric properties were compared with the ones of pure ZnO NWs and few-layer WS_2 flakes. *Fig. 5.36(a-c)* shows measured typical current-voltage characteristics of photodetectors built using pure ZnO NWs, WS_2 flakes and ZnO-WS_2 *core-shell* NWs, respectively. The ZnO photodetector demonstrates a non-symmetric I_{ds}-V_{ds} curve and this is typical for Schottky barrier of ZnO NWs on gold contacts [101]. However, nearly symmetric characteristics were obtained for WS_2 flakes and ZnO-WS_2 NW devices.

On-off photoresponse measurements were performed at the bias voltage of 1V, laser wavelengths of 405, 532 and 660 nm and laser power of 0.5 W/cm^2. Typical photoresponse measurements of pure ZnO NW, WS_2 flake and ZnO-WS_2 *core-shell* NW devices are shown in *Fig. 5.23(d-f)*. Pure ZnO NWs respond only to the illumination of 405 nm wavelength and do not respond to wavelengths of 532 and 660 nm (*Fig. 5.23(d)*), while the photoresponse of WS_2 flakes is almost identical at wavelengths of 405, 532 and 660 nm (*Fig. 5.23(e)*). The photoresponse of ZnO-WS_2 *core-shell* NWs at 532 and 660 nm are similar, but the photoresponse is significantly stronger at 405 nm (*Fig. 5.23(f)*). Since pure ZnO NWs do not respond to green 532 nm (2.33 eV) and red 660 nm (1.88 eV) light because of their wide band gap (E_g=3.2–3.3 eV), the photoresponse of ZnO-WS_2 *core-shell* NWs to red and green light can be attributed to the WS_2 shell. For violet light (405 nm), both ZnO core and WS_2 shell contribute proportionally to the photoresponse of ZnO-WS_2 *core-shell* NWs.

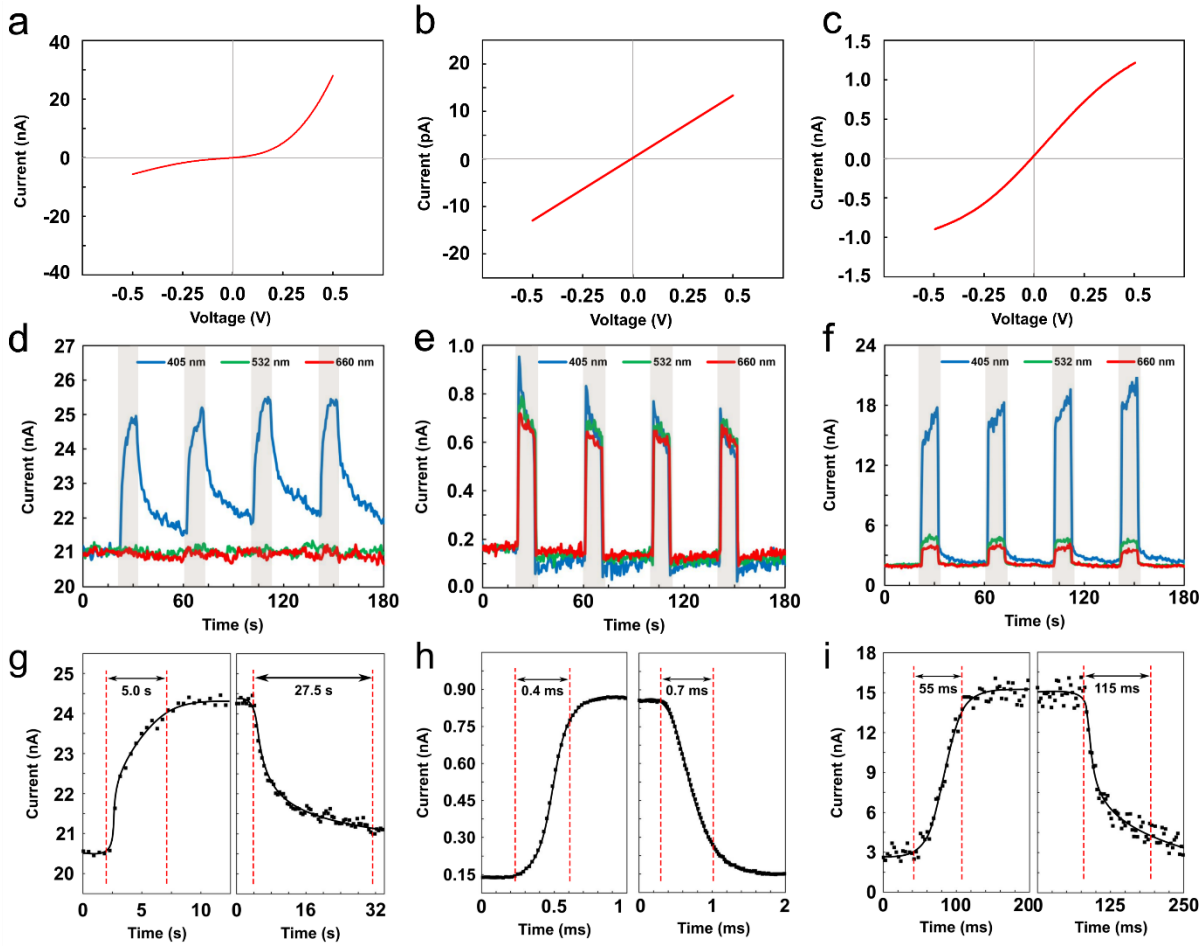

Figure 5.23. Dark-state I_{ds}-V_{ds} characteristics of (a) ZnO NW, (b) WS_2 flakes and (c) ZnO-WS_2 NW photodetectors. On-off photoresponse measurements of (d) ZnO NW, (e) WS_2 flakes and (f) ZnO-WS_2 NW photodetectors at V_{ds} = 1 V bias voltage and 0.5 W/cm^2 light intensity of 405 nm, 532 nm and 660 nm wavelength light illumination. Time-resolved photoresponse measurements of (g) ZnO NW, (h) WS_2 flakes and (i) ZnO-WS_2 NW photodetectors at V_{ds} = 1 V bias voltage and 0.5 W/cm^2 light intensity of 405 nm wavelength light illumination.

Time-resolved photoresponse measurements are presented in *Fig. 5.23(g-i)*, and the corresponding data are given in *Table 5.3*. A slow response of pure ZnO NWs on the timescale of seconds is typical for this material [52,101]. In addition, the response time of WS_2 flakes depends on the material fabrication method and the number of WS_2 layers [102,103]. Perea-López et al. reported the response time of a few layer WS_2 photodetector as fast as 5.3 ms [102], while Huo et al. reported the response time of a multilayer WS_2 photodetector to be faster than 20 ms [103]. The response time of the prepared ZnO-WS_2 *core-shell* NWs is significantly faster than that of ZnO-WS_2-based heterostructured thin film devices [104]. The calculated values of R_λ and *EQE* for the photodetectors are given in *Table 5.4*, and the obtained data are comparable to other *state-of-art* ZnO nanowire- and WS_2 nanotube-based photodetectors. For example, Guo et al. demonstrated the high responsivity of a ZnO nanowire-based UV photodetector having 40 A/W; however, at 10 V bias the kinetics of the photodetector was measured in the range of seconds [101]. In contrast, Zhang

et al. demonstrated a multiwall WS_2 nanotube-based photodetector with R_λ = 3.14 A/W (at 0.5 V bias) and *EQE* = 615% for 633 nm light [105].

Table 5.3. Photoresponse (rise and decay) time of the studied photodetectors fabricated from pure ZnO NWs, WS_2 flakes and ZnO-WS_2 *core-shell* NWs.

λ, nm	ZnO NWs		WS_2 flakes		ZnO-WS_2 NWs	
	Rise, s	Decay, s	Rise, ms	Decay, ms	Rise, ms	Decay, ms
405	5	27.5	0.4	0.7	55	115
532	-	-	0.3	0.65	21	95
660	-	-	0.53	1.35	22	50

Table 5.4. Responsivity R_λ and external quantum efficiency EQE values of the studied photodetectors fabricated from pure ZnO NWs, WS_2 flakes and ZnO-WS_2 *core-shell* NWs.

Parameters	λ, nm	ZnO NWs	WS_2 flakes	ZnO-WS_2 NWs
R_λ, A/W	405	1.50	5.03×10^{-4}	7.00
	532	-	4.84×10^{-4}	2.25
	660	-	4.58×10^{-4}	1.75
EQE, %	405	4.59	1.5×10^{-3}	21.4
	532	-	1.1×10^{-3}	5.2
	660	-	8.6×10^{-4}	3.3

5.5.3 PbI_2-decorated ZnO nanowire photodetectors

Photoelectric properties of PbI_2-decorated ZnO NWs prepared via reactive magnetron deposition of a lead oxide film followed by subsequent iodination to PbI_2 were investigated and compared to ones of hybrid nanostructures prepared via thermal evaporation method. *Fig. 5.24(a–c)* shows the characteristics of the two-terminal ZnO-PbI_2 single NW devices made using the thermal evaporation approach, while *Fig. 5.24(d–f)* shows the characteristics of the ZnO-PbI_2 single NW devices made by converting the magnetron-sputtered lead oxide coating. Both dark state current-voltage (I_{ds}-V_{ds}) characteristics of ZnO-PbI_2 NWs in *Fig. 5.24(a)* and *Fig. 5.24(d)* exhibit linear behaviour, indicating that ohmic contacts formed between the nanostructures and the electrodes, as is expected for PbI_2 on gold [106] and which is beneficial for efficient photogenerated carrier collection. In contrast, pure ZnO NWs typically form Schottky contact with gold electrodes (see the nonsymmetric I-V curve in *Fig. 5.23(a)*) [101].

The devices were illuminated with 405 nm wavelength light in a periodic fashion to study their photoresponse properties as shown in *Fig. 5.24(b)* and *Fig. 5.24(e)*. All the devices were also tested for 532 nm and 660 nm light illumination; however, no increase in current was observed due to the relatively wide bandgap of the studied materials. On-off measurements demonstrate a steady, rapid and

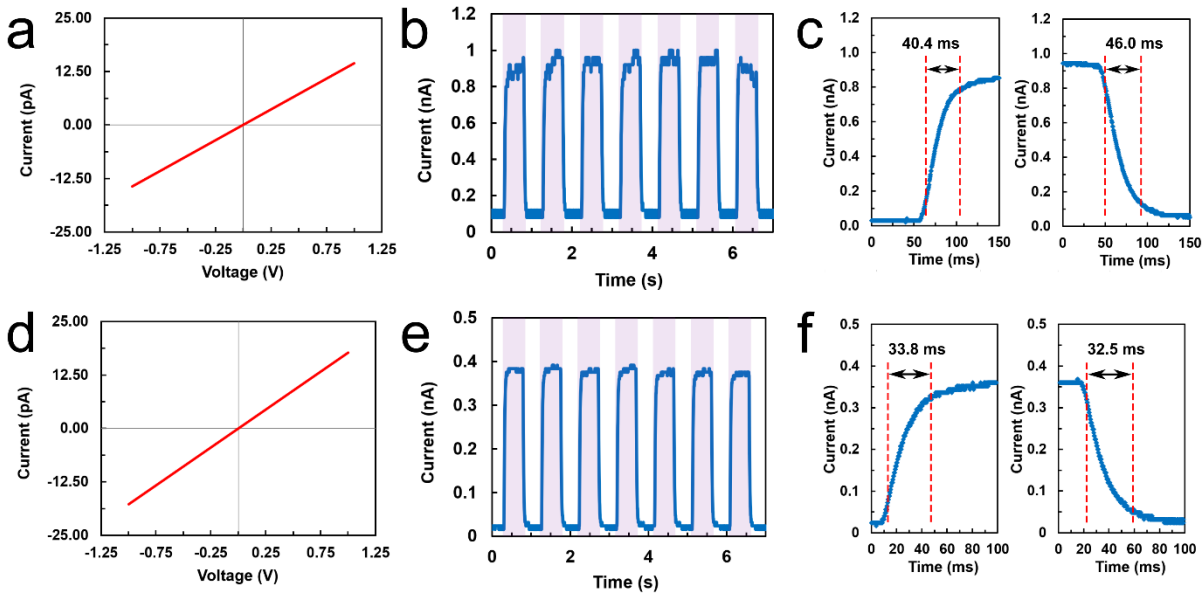

Figure 5.24. ZnO-PbI_2 single NW made by using the thermal evaporation approach (a) dark-state I_{ds}-V_{ds} characteristics, (b) on−off photoresponse, (c) time-resolved photoresponse measurements; and ZnO-PbI_2 single NW made by converting the lead oxide coating (d) dark-state I_{ds}-V_{ds} characteristics, (e) on−off photoresponse, (f) time-resolved photoresponse measurements at 1 V bias voltage and 0.5 W/cm^2 light intensity of 405 nm wavelength light.

repeatable increase and decrease of the current when the illumination is turned on or off, respectively; therefore, showing good stability and reversibility of the devices. ZnO-PbI_2 NWs exhibit low dark current (10–100 pA) which is necessary for high-performance photodetectors, while for pure ZnO NWs, it can be up to several tens of nA (see *Fig. 5.23(d)*). The current enhancement ratios (I_{on}/I_{off}) for the nanostructures prepared via both approaches were measured to be at around 10–20, in contrast to less than 2 for pure ZnO NWs.

Time-resolved photoresponse measurements were performed to evaluate the rise and decay time of the as-prepared ZnO-PbI_2 devices. As shown in *Fig. 5.24(c)* and *Fig. 5.24(f)*, the obtained values are in the 30-50 ms range, which is almost two orders of magnitude faster than the pure ZnO NWs (see *Fig. 5.23(g)*) and comparable to typical NW or 2D PbI_2 photodetector response times [14,92,93,100]. The slow response of ZnO NWs is due to the influence of oxygen molecules on the surface states and their effect on photoresponse kinetics is widely discussed in the literature [107,108].

In this work, surface of ZnO NWs was passivated using a thin PbI_2 or WS_2 coating, and photodetectors of such heterostructures exhibit reduced dark current and photoresponse time, although it also decreases on-state current I_{on} in comparison to pure ZnO NWs. It is well known that adsorbed oxygen species influence electrical properties (electrical conductivity decreases with exposure to oxygen) of metal oxide nanostructures [52,109,110]. Consequently, band bending, induced by adsorbed oxygen molecules that capture free electrons, causes an efficient photogenerated electron-hole separation that leads to high gain in single-nanowire photodetectors. The presence of the PbI_2 layers in the nanostructures protects the ZnO surface from

oxygen adsorption that might influence surface-related photoinduced processes and decrease the number of charge carrier trapping centres.

A responsivity as high as ~0.6 A/W (EQE ~180%) was calculated for the ZnO-PbI_2 single NW devices made using the thermal evaporation approach and ~0.3 A/W (EQE ~90%) for the ones made by converting the magnetron-sputtered lead oxide coating; however, it is not valid to compare the two different synthesis approaches based only on the responsivity values as the value range for all as-fabricated devices overlapped no matter which method was used. The obtained R_λ and EQE values are comparable to other typical *state-of-the-art* 1D nanostructure [100] and 2D PbI_2 [92,93,111] photodetectors.

6. CONCLUSIONS AND THESIS

In this work, development and characterization of various material nanowire and transition metal dichalcogenide *core-shell* heterostructures was demonstrated, including investigation of the nanostructure photoelectric properties.

The synthesis methods developed in this work are not limited to the demonstrated heterostructures and can be applied for other materials, if their compatibility is considered. Numerous other combinations of materials have also been investigated, and it was concluded that: 1) the sulfurization of the sacrificial shell material must occur at a lower temperature than that of the NW core recrystallization temperature; 2) to grow the layered material parallelly and uniformly around the NW, usually the symmetry and the material lattice parameters should be similar, otherwise the layered material grows out-of-plane or as islands, with specific exceptions. Therefore, if the criteria are met, the novel method is quite versatile - many layered materials might be grown with such method, if the right NW material is selected. Here, it has been demonstrated that high-quality layered materials can be grown around single crystal NWs parallel to the substrate NW surface plane.

In most of the cases, the shell thickness is not symmetrical on both sides of NWs. This is mainly due to different angular distribution of nanowires during magnetron deposition of the precursor material – nanowires oriented perpendicular to substrate plane are covered more homogeneously, while for nanowires oriented horizontally the upper side is covered with more material compared to the bottom side. For vertically oriented nanowires with length up to 10-20 μm, the coverage should be homogenous. Precursor deposition via the salt solution immersion method exhibits much more uniform shell thickness that does not depend on the NW orientation, in contrast to the magnetron deposition. With finely tuned process parameters, such as pre-deposited oxide thickness, NW length and orientation, temperature, sulfur vapour and carrier gas flow, precise control over the number of layers should be achievable with the proposed methods.

ZnO NWs were of particular interest in this work due to the pronounced change of their photoelectric properties after the surface modification. By fabricating two-terminal single-nanowire photodetectors from the NW heterostructures, it was shown that few layers of WS_2 or PbI_2 can significantly affect photoconductive properties of ZnO NWs. For example, ZnO-WS_2 *core-shell* NW two-terminal devices exhibit enhanced spectral responsivity in comparison to pure ZnO NWs, and light absorption in the WS_2 shell extends the active spectral range to the red part of the spectrum. Notably, ZnO NW surface passivation with layered vdW materials shell improves their photoresponse time for almost two orders of magnitude due to thus limited photo-induced processes related to adsorption/desorption of atmospheric oxygen species which typically slows down photoresponse in ZnO NWs. Therefore, fast operation of NW-based photodetectors might be achieved using such *core-shell* materials.

Two-terminal photodetectors based on the as-prepared *core-shell* NWs are comparable to other *state-of-the-art* 1D and 2D nanostructure photodetectors reported in literature. However, the combination of different materials in more complex hybrid NWs gives extra freedom to flexibly design their properties and add

custom-made functionality. Such novel heterostructures could also be used for other applications in optoelectronics and in photo- or electrocatalytic hydrogen evolution reactions, which can be assumed from the favourable heterostructure band alignment.

Thesis

1. Few-layer WS_2 can be epitaxially grown on ZnO nanowires at 800°C by sulfurization of a WO_3 coating, pre-deposited on nanowires via reactive magnetron sputtering. The WS_2 shell enhances ZnO nanowire photosensitivity in the short wavelength range (spectral responsivity increases from 1.5 A/W to 7.0 A/W at 405 nm, dark current remains similar) and extends the spectral range to the red part of the spectrum. ZnO nanowire surface passivation with few-layer WS_2 improves photoresponse time for almost two orders of magnitude from several seconds to tens of miliseconds.
2. Few-layer PbI_2 was synthesised using a new method – iodination at 420°C of a PbO_x coating, pre-deposited via reactive magnetron sputtering. ZnO nanowire decoration with few-layer PbI_2 leads to significantly decreased dark current (from several nanoamperes to tens of picoamperes) at a cost of slightly reduced spectral responsivity from 1.5 A/W to 0.6 A/W at 405 nm. ZnO nanowire surface passivation with few-layer PbI_2 decreases photoresponse time by more than one order of magnitude from several seconds to tens of miliseconds.
3. Decomposition and sulfurization at 700°C of an ammonium heptamolybdate tetrahydrate coating, pre-deposited on ZnO nanowires via solution immersion, was found to be a viable method for ZnO-MoS_2 *core-shell* nanowire synthesis. Compared with similar two-step method of magnetron-sputtered MoO_3 coating conversion, the immersion method of molybdenum precursor deposition yields significantly thinner and more uniform few-layer MoS_2 shell compared to sputter-deposited MoO_3.
4. Preparation of novel GaN-ReS_2, ZnS-ReS_2 and ZnO-ReS_2 *core-shell* nanowire heterostructures was demonstrated using new few-layer ReS_2 synthesis method – sulfurization at 800°C of a ReO_x coating, pre-deposited via reactive magnetron sputtering. ZnO nanowire recrystallization and conversion to ZnS phase was observed at the temperature necessary for highly-crystalline ReS_2 growth. GaN and ZnS nanowires were found to be stable for the *core-shell* heterostructure synthesis, however, the ReS_2 shell crystalline quality was lower than that on the recrystallized ZnO substrate.

REFERENCES

[1] Dasgupta, N. P. *et al.* 25th Anniversary Article: Semiconductor Nanowires - Synthesis, Characterization, and Applications. *Adv. Mater.* **26**, 2137–2184 (2014)

[2] Fan, Z. *et al.* Toward the Development of Printable Nanowire Electronics and Sensors. *Adv. Mater.* **21**, 3730–3743 (2009)

[3] Yang, P., Yan, R. & Fardy, M. Semiconductor Nanowire: What's Next? *Nano Lett.* **10**, 1529–1536 (2010)

[4] Sun, Y., Sun, B., He, J. & Wang, C. Compositional and structural engineering of inorganic nanowires toward advanced properties and applications. *InfoMat* **1**, 496–524 (2019)

[5] Lauhon, L. J., Gudiksen, M. S., Wang, D. & Lieber, C. M. Epitaxial core–shell and core–multishell nanowire heterostructures. *Nature* **420**, 57–61 (2002)

[6] Dong, Y., Tian, B., Kempa, T. J. & Lieber, C. M. Coaxial Group III−Nitride Nanowire Photovoltaics. *Nano Lett.* **9**, 2183–2187 (2009)

[7] Chhowalla, M. *et al.* The chemistry of two-dimensional layered transition metal dichalcogenide nanosheets. *Nat. Chem.* **5**, 263–275 (2013)

[8] Choi, W. *et al.* Recent development of two-dimensional transition metal dichalcogenides and their applications. *Mater. Today* **20**, 116–130 (2017)

[9] Walsh, L. A. & Hinkle, C. L. van der Waals epitaxy: 2D materials and topological insulators. *Appl. Mater. Today* **9**, 504–515 (2017)

[10] Duong, D. L., Yun, S. J. & Lee, Y. H. van der Waals Layered Materials: Opportunities and Challenges. *ACS Nano* **11**, 11803–11830 (2017)

[11] Wang, Q. H., Kalantar-Zadeh, K., Kis, A., Coleman, J. N. & Strano, M. S. Electronics and optoelectronics of two-dimensional transition metal dichalcogenides. *Nat. Nanotechnol.* **7**, 699–712 (2012)

[12] Mak, K. F., Lee, C., Hone, J., Shan, J. & Heinz, T. F. Atomically thin MoS2: A new direct-gap semiconductor. *Phys. Rev. Lett.* **105**, 2–5 (2010)

[13] Splendiani, A. *et al.* Emerging Photoluminescence in Monolayer MoS2. *Nano Lett.* **10**, 1271–1275 (2010)

[14] Zhong, M. *et al.* Large-scale 2D PbI2 monolayers: experimental realization and their indirect band-gap related properties. *Nanoscale* **9**, 3736–3741 (2017)

[15] Toulouse, A. S. *et al.* Frenkel-like Wannier-Mott excitons in few-layer PbI2. *Phys. Rev. B* **91**, 165308 (2015)

[16] Zhang, E. *et al.* ReS2-Based Field-Effect Transistors and Photodetectors. *Adv. Funct. Mater.* **25**, 4076–4082 (2015)

[17] Bertolazzi, S., Brivio, J. & Kis, A. Stretching and Breaking of Ultrathin MoS2. *ACS Nano* **5**, 9703–9709 (2011)

[18] Yi, F. *et al.* Wearable energy sources based on 2D materials. *Chem. Soc. Rev.* **47**, 3152–3188 (2018)

[19] Kelly, A. G. *et al.* All-printed thin-film transistors from networks of liquid-exfoliated nanosheets. *Science (80-.).* **356**, 69–73 (2017)

[20] Gupta, A., Sakthivel, T. & Seal, S. Recent development in 2D materials beyond

graphene. *Prog. Mater. Sci.* **73**, 44–126 (2015)

[21] Coleman, J. N. *et al.* Two-dimensional nanosheets produced by liquid exfoliation of layered materials. *Science (80-.).* **331**, 568–571 (2011)

[22] Backes, C. *et al.* Guidelines for Exfoliation, Characterization and Processing of Layered Materials Produced by Liquid Exfoliation. *Chem. Mater.* **29**, 243–255 (2017)

[23] Nicolosi, V., Chhowalla, M., Kanatzidis, M. G., Strano, M. S. & Coleman, J. N. Liquid Exfoliation of Layered Materials. *Science (80-.).* **340**, 1226419–1226419 (2013)

[24] Zhang, X., Lai, Z., Tan, C. & Zhang, H. Solution-Processed Two-Dimensional MoS2 Nanosheets: Preparation, Hybridization, and Applications. *Angew. Chemie Int. Ed.* **55**, 8816–8838 (2016)

[25] Hu, G. *et al.* Functional inks and printing of two-dimensional materials. *Chem. Soc. Rev.* **47**, 3265–3300 (2018)

[26] Shi, Y., Li, H. & Li, L. J. Recent advances in controlled synthesis of two-dimensional transition metal dichalcogenides via vapour deposition techniques. *Chem. Soc. Rev.* **44**, 2744–2756 (2015)

[27] Chen, P., Zhang, Z., Duan, X. & Duan, X. Chemical synthesis of two-dimensional atomic crystals, heterostructures and superlattices. *Chem. Soc. Rev.* **47**, 3129–3151 (2018)

[28] Cong, C. *et al.* Synthesis and Optical Properties of Large-Area Single-Crystalline 2D Semiconductor WS2 Monolayer from Chemical Vapor Deposition. *Adv. Opt. Mater.* **2**, 131–136 (2014)

[29] Van Der Zande, A. M. *et al.* Grains and grain boundaries in highly crystalline monolayer molybdenum disulphide. *Nat. Mater.* **12**, 554–561 (2013)

[30] Kang, K. *et al.* High-mobility three-atom-thick semiconducting films with wafer-scale homogeneity. *Nature* **520**, 656–660 (2015)

[31] Gutiérrez, H. R. *et al.* Extraordinary Room-Temperature Photoluminescence in Triangular WS2 Monolayers. *Nano Lett.* **13**, 3447–3454 (2013)

[32] Lin, Y.-C. *et al.* Wafer-scale MoS2 thin layers prepared by MoO3 sulfurization. *Nanoscale* **4**, 6637 (2012)

[33] Wu, C.-R. *et al.* Establishment of 2D Crystal Heterostructures by Sulfurization of Sequential Transition Metal Depositions: Preparation, Characterization, and Selective Growth. *Nano Lett.* **16**, 7093–7097 (2016)

[34] Bark, H. *et al.* Large-area niobium disulfide thin films as transparent electrodes for devices based on two-dimensional materials. *Nanoscale* **10**, 1056–1062 (2018)

[35] Liu, K. K. *et al.* Growth of large-area and highly crystalline MoS2 thin layers on insulating substrates. *Nano Lett.* **12**, 1538–1544 (2012)

[36] Bakti Utama, M. I. *et al.* Recent developments and future directions in the growth of nanostructures by van der Waals epitaxy. *Nanoscale* **5**, 3570 (2013)

[37] Koma, A. Van der Waals epitaxy-a new epitaxial growth method for a highly lattice-mismatched system. *Thin Solid Films* **216**, 72–76 (1992)

[38] Xie, C., Mak, C., Tao, X. & Yan, F. Photodetectors Based on Two-Dimensional

Layered Materials Beyond Graphene. *Adv. Funct. Mater.* **27**, (2017)

[39] Yan, F. *et al.* Toward High-Performance Photodetectors Based on 2D Materials: Strategy on Methods. *Small Methods* **2**, 1700349 (2018)

[40] Novoselov, K. S., Mishchenko, A., Carvalho, A. & Castro Neto, A. H. 2D materials and van der Waals heterostructures. *Science (80-.).* **353**, aac9439 (2016)

[41] Kang, K. *et al.* Layer-by-layer assembly of two-dimensional materials into wafer-scale heterostructures. *Nature* **550**, 229–233 (2017)

[42] Wang, F. *et al.* Progress on Electronic and Optoelectronic Devices of 2D Layered Semiconducting Materials. *Small* **13**, 1604298 (2017)

[43] Zhao, Y. *et al.* Doping, Contact and Interface Engineering of Two-Dimensional Layered Transition Metal Dichalcogenides Transistors. *Adv. Funct. Mater.* **27**, (2017)

[44] Xie, L. M. Two-dimensional transition metal dichalcogenide alloys: preparation, characterization and applications. *Nanoscale* **7**, 18392–18401 (2015)

[45] Schulman, D. S., Arnold, A. J. & Das, S. Contact engineering for 2D materials and devices. *Chem. Soc. Rev.* **47**, 3037–3058 (2018)

[46] Farmanbar, M. & Brocks, G. Ohmic Contacts to 2D Semiconductors through van der Waals Bonding. *Adv. Electron. Mater.* **2**, 1500405 (2016)

[47] Schaibley, J. R. *et al.* Valleytronics in 2D materials. *Nat. Rev. Mater.* **1**, 1–15 (2016)

[48] Sorger, V. J., Oulton, R. F., Ma, R.-M. & Zhang, X. Toward integrated plasmonic circuits. *MRS Bull.* **37**, 728–738 (2012)

[49] Sannicolo, T. *et al.* Metallic Nanowire-Based Transparent Electrodes for Next Generation Flexible Devices: a Review. *Small* **12**, 6052–6075 (2016)

[50] Long, Y.-Z., Yu, M., Sun, B., Gu, C.-Z. & Fan, Z. Recent advances in large-scale assembly of semiconducting inorganic nanowires and nanofibers for electronics, sensors and photovoltaics. *Chem. Soc. Rev.* **41**, 4560 (2012)

[51] Law, M., Goldberger, J. & Yang, P. Semiconductor Nanowires and Nanotubes. *Annu. Rev. Mater. Res.* **34**, 83–122 (2004)

[52] Soci, C. *et al.* ZnO Nanowire UV Photodetectors with High Internal Gain. *Nano Lett.* **7**, 1003–1009 (2007)

[53] Gogurla, N., Sinha, A. K., Santra, S., Manna, S. & Ray, S. K. Multifunctional Au-ZnO Plasmonic Nanostructures for Enhanced UV Photodetector and Room Temperature NO Sensing Devices. *Sci. Rep.* **4**, 6483 (2015)

[54] Deng, K. & Li, L. CdS Nanoscale Photodetectors. *Adv. Mater.* **26**, 2619–2635 (2014)

[55] Xie, X. & Shen, G. Single-crystalline In2S3 nanowire-based flexible visible-light photodetectors with an ultra-high photoresponse. *Nanoscale* **7**, 5046–5052 (2015)

[56] Soci, C. *et al.* Nanowire Photodetectors. *J. Nanosci. Nanotechnol.* **10**, 1430–1449 (2010)

[57] Hayden, O., Greytak, A. B. & Bell, D. C. Core-shell nanowire light-emitting diodes. *Adv. Mater.* **17**, 701–704 (2005)

[58] Adachi, M. M., Anantram, M. P. & Karim, K. S. Core-shell silicon nanowire solar cells. *Sci. Rep.* **3**, 1546 (2013)

[59] Vlassov, S. *et al.* Shape Restoration Effect in Ag–SiO2 Core–Shell Nanowires. *Nano Lett.* **14**, 5201–5205 (2014)

[60] Liu, X. W., Hu, J. & Pan, B. C. The composition-dependent mechanical properties of Ge/Si core–shell nanowires. *Phys. E Low-dimensional Syst. Nanostructures* **40**, 3042–3048 (2008)

[61] Dan, Y. *et al.* Dramatic reduction of surface recombination by in situ surface passivation of silicon nanowires. *Nano Lett.* **11**, 2527–2532 (2011)

[62] Barth, S., Hernandez-Ramirez, F., Holmes, J. D. & Romano-Rodriguez, A. Synthesis and applications of one-dimensional semiconductors. *Prog. Mater. Sci.* **55**, 563–627 (2010)

[63] Mieszawska, A. J., Jalilian, R., Sumanasekera, G. U. & Zamborini, F. P. The synthesis and fabrication of one-dimensional nanoscale heterojunctions. *Small* **3**, 722–756 (2007)

[64] Han, S. *et al.* Transition Metal Oxide Core−Shell Nanowires: Generic Synthesis and Transport Studies. *Nano Lett.* **4**, 1241–1246 (2004)

[65] Fontcuberta i Morral, A. *et al.* Prismatic Quantum Heterostructures Synthesized on Molecular-Beam Epitaxy GaAs Nanowires. *Small* **4**, 899–903 (2008)

[66] Yu, H., Liu, C. M., Huang, X. Y. & Lei, M. Y. The microstructure and photoluminescence of ZnO–MoS2 core shell nano-materials. *Mater. Res. Express* **4**, 015024 (2017)

[67] Chen, F., Wang, T., Wang, L., Ji, X. & Zhang, Q. Improved light emission of MoS2 monolayers by constructing AlN/MoS2 core–shell nanowires. *J. Mater. Chem. C* **5**, 10225–10230 (2017)

[68] Seo, B., Jeong, H. Y., Hong, S. Y., Zak, A. & Joo, S. H. Impact of a conductive oxide core in tungsten sulfide-based nanostructures on the hydrogen evolution reaction. *Chem. Commun.* **51**, 8334–8337 (2015)

[69] Zhang, L., Liu, C., Wong, A. B., Resasco, J. & Yang, P. MoS2-wrapped silicon nanowires for photoelectrochemical water reduction. *Nano Res.* **8**, 281–287 (2014)

[70] Chen, Z. *et al.* Core–shell MoO3 –MoS2 Nanowires for Hydrogen Evolution: A Functional Design for Electrocatalytic Materials. *Nano Lett.* **11**, 4168–4175 (2011)

[71] Klinger, M. More features, more tools, more CrysTBox. *J. Appl. Crystallogr.* **50**, 1226–1234 (2017)

[72] Peimyoo, N. *et al.* Nonblinking, intense two-dimensional light emitter: Monolayer WS2 Triangles. *ACS Nano* **7**, 10985–10994 (2013)

[73] Elías, A. L. *et al.* Controlled synthesis and transfer of large-area WS2 sheets: From single layer to few layers. *ACS Nano* **7**, 5235–5242 (2013)

[74] Lien, D.-H. *et al.* Large-area and bright pulsed electroluminescence in monolayer semiconductors. *Nat. Commun.* **9**, 1229 (2018)

[75] Polyakov, B. *et al.* Unexpected Epitaxial Growth of a Few WS2 Layers on $\{1\bar{1}00\}$ Facets of ZnO Nanowires. *J. Phys. Chem. C* **120**, 21451–21459 (2016)

[76] Krause, M., Mücklich, A., Zak, A., Seifert, G. & Gemming, S. High resolution TEM study of WS2 nanotubes. *Phys. Status Solidi Basic Res.* (2011) doi:10.1002/pssb.201100076

[77] Butanovs, E. *et al.* Fast-Response Single-Nanowire Photodetector Based on ZnO/WS2 Core/Shell Heterostructures. *ACS Appl. Mater. Interfaces* **10**, 13869–13876 (2018)

[78] Özgür, Ü. *et al.* A comprehensive review of ZnO materials and devices. *J. Appl. Phys.* **98**, 041301 (2005)

[79] Rahman, M., Davey, K. & Qiao, S.-Z. Advent of 2D Rhenium Disulfide (ReS2): Fundamentals to Applications. *Adv. Funct. Mater.* **27**, 1606129 (2017)

[80] Gong, C. *et al.* Electronic and Optoelectronic Applications Based on 2D Novel Anisotropic Transition Metal Dichalcogenides. *Adv. Sci.* **4**, 1700231 (2017)

[81] Lin, Y.-C. *et al.* Single-Layer ReS2: Two-Dimensional Semiconductor with Tunable In-Plane Anisotropy. *ACS Nano* **9**, 11249–11257 (2015)

[82] He, X. *et al.* Chemical Vapor Deposition of High-Quality and Atomically Layered ReS2. *Small* **11**, 5423–5429 (2015)

[83] Qin, J.-K. *et al.* van der Waals epitaxy of large-area continuous ReS2 films on mica substrate. *RSC Adv.* **7**, 24188–24194 (2017)

[84] Urakami, N., Okuda, T. & Hashimoto, Y. Epitaxial growth of ReS2 (001) thin film via deposited-Re sulfurization. *Jpn. J. Appl. Phys.* **57**, 02CB07 (2018)

[85] Ho, C. ., Huang, Y. ., Liao, P. . & Tiong, K. . Crystal structure and band-edge transitions of ReS2−xSex layered compounds. *J. Phys. Chem. Solids* **60**, 1797–1804 (1999)

[86] Butanovs, E., Kuzmin, A., Butikova, J., Vlassov, S. & Polyakov, B. Synthesis and characterization of ZnO/ZnS/MoS2 core-shell nanowires. *J. Cryst. Growth* **459**, 100–104 (2017)

[87] Panda, S. K., Dev, A. & Chaudhuri, S. Fabrication and Luminescent Properties of c-Axis Oriented ZnO−ZnS Core−Shell and ZnS Nanorod Arrays by Sulfidation of Aligned ZnO Nanorod Arrays. *J. Phys. Chem. C* **111**, 5039–5043 (2007)

[88] Feng, Y. *et al.* Raman vibrational spectra of bulk to monolayer ReS2 with lower symmetry. *Phys. Rev. B* **92**, 054110 (2015)

[89] Tonndorf, P. *et al.* Photoluminescence emission and Raman response of monolayer MoS2, MoSe2, and WSe2. *Opt. Express* **21**, 4908 (2013)

[90] Zhang, J. *et al.* Layered ultrathin PbI2 single crystals for high sensitivity flexible photodetectors. *J. Mater. Chem. C* **3**, 4402–4406 (2015)

[91] Sun, H. *et al.* Laser-induced surface recrystallization of polycrystalline PbI2 thick films for X-ray detector application. *Appl. Surf. Sci.* **427**, 1146–1151 (2018)

[92] Zheng, W. *et al.* High-Crystalline 2D Layered PbI2 with Ultrasmooth Surface: Liquid-Phase Synthesis and Application of High-Speed Photon Detection. *Adv. Electron. Mater.* **2**, 1600291 (2016)

[93] Wang, Y., Gan, L., Chen, J., Yang, R. & Zhai, T. Achieving highly uniform two-dimensional PbI2 flakes for photodetectors via space confined physical vapor deposition. *Sci. Bull.* **62**, 1654–1662 (2017)

[94] Butanovs, E., Piskunov, S., Zolotarjovs, A. & Polyakov, B. Growth and characterization of PbI2-decorated ZnO nanowires for photodetection applications. *J. Alloys Compd.* **825**, 154095 (2020)

[95] Condeles, J. F., Ando, R. A. & Mulato, M. Optical and structural properties of PbI2 thin films. *J. Mater. Sci.* **43**, 525–529 (2008)

[96] Butanovs, E., Butikova, J., Zolotarjovs, A. & Polyakov, B. Towards metal chalcogenide nanowire-based colour-sensitive photodetectors. *Opt. Mater. (Amst).* **75**, 501–507 (2018)

[97] Talin, A. A., Léonard, F., Swartzentruber, B. S., Wang, X. & Hersee, S. D. Unusually Strong Space-Charge-Limited Current in Thin Wires. *Phys. Rev. Lett.* **101**, 076802 (2008)

[98] Katzenmeyer, A. M. *et al.* Observation of Space-Charge-Limited Transport in InAs Nanowires. *IEEE Trans. Nanotechnol.* **10**, 92–95 (2011)

[99] Vilà, A. *et al.* Fabrication of metallic contacts to nanometre-sized materials using a focused ion beam (FIB). *Mater. Sci. Eng. C* **26**, 1063–1066 (2006)

[100] Zhai, T. *et al.* Recent Developments in One-Dimensional Inorganic Nanostructures for Photodetectors. *Adv. Funct. Mater.* **20**, 4233–4248 (2010)

[101] Lao, C. S. *et al.* ZnO Nanobelt/Nanowire Schottky Diodes Formed by Dielectrophoresis Alignment across Au Electrodes. *Nano Lett.* **6**, 263–266 (2006)

[102] Perea-López, N. *et al.* Photosensor Device Based on Few-Layered WS2 Films. *Adv. Funct. Mater.* **23**, 5511–5517 (2013)

[103] Huo, N. *et al.* Photoresponsive and Gas Sensing Field-Effect Transistors based on Multilayer WS2 Nanoflakes. *Sci. Rep.* **4**, 5209 (2015)

[104] Lan, C. *et al.* ZnO–WS2 heterostructures for enhanced ultra-violet photodetectors. *RSC Adv.* **6**, 67520–67524 (2016)

[105] Zhang, C. *et al.* High-performance photodetectors for visible and near-infrared lights based on individual WS2 nanotubes. *Appl. Phys. Lett.* **100**, 243101 (2012)

[106] Zhong, M. *et al.* Flexible photodetectors based on phase dependent PbI2 single crystals. *J. Mater. Chem. C* **4**, 6492–6499 (2016)

[107] Cheng, G. *et al.* ZnO nanowire Schottky barrier ultraviolet photodetector with high sensitivity and fast recovery speed. *Appl. Phys. Lett.* **99**, 203105 (2011)

[108] Mallampati, B., Nair, S. V., Ruda, H. E. & Philipose, U. Role of surface in high photoconductive gain measured in ZnO nanowire-based photodetector. *J. Nanoparticle Res.* **17**, 176 (2015)

[109] Wu, J.-M. & Kuo, C.-H. Ultraviolet photodetectors made from SnO2 nanowires. *Thin Solid Films* **517**, 3870–3873 (2009)

[110] Yamazoe, N., Fuchigami, J., Kishikawa, M. & Seiyama, T. Interactions of tin oxide surface with O2, H2O AND H2. *Surf. Sci.* **86**, 335–344 (1979)

[111] Zhang, J. *et al.* Low-Temperature Heteroepitaxy of 2D PbI 2 /Graphene for Large-Area Flexible Photodetectors. *Adv. Mater.* **30**, 1803194 (2018)

LIST OF PUBLICATIONS

Included in Dissertation:

I. **E. Butanovs,** S. Piskunov, A. Zolotarjovs, B. Polyakov. Growth and characterization of PbI2-decorated ZnO nanowires for photodetection applications. *J. Alloys Compd.* 825, 154095 (2020)

II. **E. Butanovs**, S. Vlassov, A. Kuzmin, S. Piskunov, J. Butikova, B. Polyakov. Fast-response single-nanowire photodetector based on ZnO/WS2 core/shell heterostructures. *ACS Appl. Mater. Interfaces*. 10, 13869-13876 (2018)

III. **E. Butanovs**, J. Butikova, A. Zolotarjovs, B. Polyakov. Towards metal chalcogenide nanowire-based colour-sensitive photodetectors. *Opt. Mater.* 75, 501–507 (2018)

IV. **E. Butanovs**, A. Kuzmin, J. Butikova, S. Vlassov, K. Smits, B. Polyakov. Synthesis and characterization of ZnO/ZnS/MoS2 core-shell nanowires. *J. Crys. Growth*. 459, 100-104 (2017)

V. B. Polyakov, K. Smits, A. Kuzmin, J. Zideluns, **E. Butanovs**, J. Butikova, S. Vlassov, S. Piskunov, Y. Zhukovskii. Unexpected epitaxial growth of a few WS2 layers on $\{1\bar{1}00\}$ facets of ZnO nanowires. *J. Phys. Chem. C.* 120, 21451-21459 (2016)

VI. **E. Butanovs**, A. Kuzmin, S. Piskunov, K. Smits, A. Kalinko, B. Polyakov. Synthesis and characterization of GaN/ReS2, ZnS/ReS2 and ZnO/ReS2 core/shell nanowire heterostructures. *Submitted manuscript*.

Other publications:

B. Polyakov, A. Kuzmin, S. Vlassov, **E. Butanovs**, J. Zideluns, J. Butikova, R. Kalendarev, M. Zubkins. Production and characterisation of heterostructured CuO/CuWO4 nanowires and thin films. *J. Crys. Growth,* 480, 78–84 (2017)

J. Butikova, B. Polyakov, L. Dimitrocenko, **E. Butanovs**, I. Tale. Laser scribing on HOPG for graphene stamp printing on silicon wafer. *Central European Journal of Physics*. 11, 580-583 (2013)

Author's contribution to publications

Paper I: Corresponding author, body of the article written; materials synthesis; SEM, XRD measurements; device fabrication and characterization.

Paper II: Parts of the article written; materials synthesis; device fabrication and characterization.

Paper III: Corresponding author, body of the article written; materials synthesis; SEM measurements; device fabrication and characterization.

Paper IV: Parts of the article written; materials synthesis.

Paper V: Materials synthesis.

Paper VI: Corresponding author, body of the article written; materials synthesis; SEM, XRD measurements.

PARTICIPATION IN SUMMER SCHOOLS AND CONFERENCES

Summer Schools:

1. "European School On Nanosciences & Nanotechnologies 2019 (ESONN-2019)". Grenoble, France, August 25th – September 14th 2019.

2. Summer School "Optoelectronics on 2D materials". Davos, Switzerland, August 20th – 25th 2018.

Conferences:

1. International conference "Functional materials and nanotechnologies 2018 (FM&NT-2018)". Poster presentation: "ZnO/WS_2 nanowire core/shell heterostructures for light detection". Riga, October 2018.

2. ISSP, University of Latvia 34th Scientific Conference. Oral presentation: "1D and 2D ReS_2-based nanostructure photodetectors". Riga, February 2018

3. International conference "Functional materials and nanotechnologies 2017 (FM&NT-2017)". Poster presentation: "Engineering of metal sulfide nanowire photoresistors". Tartu, April 2017.

4. 13th International Young Scientist conference "Developments in Optics and Communications 2017". Poster presentation: "Engineering of metal sulfide nanowire photoresistors". Riga, April 2017.

5. ISSP, University of Latvia 33th Scientific Conference. Oral presentation: "Engineering of metal sulfide nanowire photodetectors". Riga, February 2017.

6. Member in the local organizing committee and participation in "The Second European Workshop on Understanding and Controlling Nano and Mesoscale Friction". Riga, July 2016.

7. 12th International Young Scientist conference "Developments in Optics and Communications 2016". Poster presentation: "Photoluminescence in 2D transition metal dichalcogenide nanostructures". Riga, March 2016.

8. ISSP, University of Latvia 32th Scientific Conference. Oral presentation: "2D transition metal dichalcogenide nanocrystals". Riga, February 2016.

9. International symposium RCBJSF-2014-FMNT. Poster presentation: "HOPG patterning methods for graphene transferring onto the substrate". Riga, September 2014.

10. ISSP, University of Latvia 30th Scientific Conference. Oral presentation: "HOPG patterning methods for graphene stamp printing on silicon wafer". Riga, February 2014.

11. ISSP, University of Latvia 29th Scientific Conference. Oral presentation: "Laser scribing on HOPG for graphene stamp printing on silicon wafer". Riga, February 2013.

ACKNOWLEDGEMENTS

I would like to express my greatest gratitude to Dr. Boris Polyakov for supervising my bachelor, master and PhD thesis, for introducing me to the field of nanotechnologies, for teaching me philosophy of science and so many experimental techniques and tricks. Thank you for the long-term contribution to my scientific development!

I would like to thank all my colleagues from Thin Film laboratory and Laboratory of Semiconductor Optoelectronics for help and the given knowledge over the years. Special thanks to Dr. Alexei Kuzmin for Raman measurements, Aleksejs Zolotarjovs for photoluminescence measurements, Dr. Krišjānis Šmits for assistance with TEM and SAED measurements, Dr. Sergei Piskunov for DFT calculations, Dr. Edgars Nitišs and Dr. Roberts Rimša for teaching me lithography steps.

I would like to thank my family for the support throughout my studies. I owe great gratitude to my friends for the support, especially Arturs Bundulis for many great discussions we had, Agnese Čikule and Sindija Balode for actively motivating me to work harder and write my Dissertation.

I would like to acknowledge financial support from Latvian National Research Program IMIS2, Scientific Research Projects for Students and Young Researchers No. SJZ/2016/6, No. SJZ/2017/1 and No. SJZ/2018/7 realized at the Institute of Solid State Physics, University of Latvia, and Latvian Council of Science grants LZP FLPP No. lzp-2018/2-0353 and No. lzp-2018/2-0083.